Study of ZnO nanocrystals with different oxygen vacancy concentrations using High Resolution Electron Energy Loss Spectroscopy

A thesis submitted

in partial fulfilment for the degree of

Master of Science

as a part of the

Integrated Ph.D. Programme
(Materials Science)

by

Dileep Krishnan

International Centre for Materials Science
Chemistry and Physics of Materials Unit
Jawaharlal Nehru Centre for Advanced Scientific Research
(A Deemed University)
Bangalore, India.
March 2011

Dedicated

to my parents

DECLARATION

I hereby declare that the matter embodied in the thesis entitled "**Study of ZnO nanocrystals with different oxygen vacancy concentrations using High Resolution Electron Energy Loss Spectroscopy**" is the result of investigations carried out by me at the International Center for Materials Science, Jawaharlal Nehru Centre for Advanced Scientific Research, India under the supervision of Dr. Ranjan Datta and that it has not been submitted elsewhere for the award of any degree or diploma.

In keeping with the general practice in reporting the scientific observations, due acknowledgement has been made whenever the work described is based on the findings of other investigators. Any omission that might have occurred due to oversight or error in judgement is regretted.

Dileep Krishnan

CERTIFICATE

I hereby certify that the work described in this thesis entitled "**Study of ZnO nanocrystals with different oxygen vacancy concentrations using High Resolution Electron Energy Loss Spectroscopy**" has been carried out by Mr. Dileep Krishnan under my supervision at the International Center for Materials Science, Jawaharlal Nehru Centre for Advanced Scientific Research, India and that it has not been submitted elsewhere for the award of any degree or diploma.

Dr. Ranjan Datta

ACKNOWLEDGEMENT

I am very pleased to acknowledge my research supervisor Dr. Ranjan Datta who gave an opportunity to work on the field of semiconductor oxides, transmission electron microscopy and spectroscopy. His simple way of thinking about a problem always inspires me a lot. I shall remain ever thankful to him for giving me enough freedom to work on my own area of interests.

I thank Prof. U.V. Waghmare for helping us with fruitful discussion and inspiring us in the theoretical calculations.

I am very grateful to Dr. K. P. S.S. Hembram for helping me and giving valuable tips for the theoretical calculations.

I especially thank my Lab mates Loukya Chowdary, Sireesha Kanuri and P. Sowjanya for creating the perfect ambience in the lab for wonderful working. I thank Dr. Karthick Balasubramanian, the application specialist from Icon Analytical for his valuable help during the experiments. I am grateful to L. S. Panchakarla for providing samples for the study. I thank Claudy Ryan Serrao for providing training in pulsed laser deposition technique. I than Dr. A. Govindaraj for his supports and helps during experiments.

I shall be ever thankful to Prof. G. U. Kulkarni, Prof. S**.** Balasubramanian**,** Prof. A. Sundaresan, Prof. S. M. Shivaprasad, Prof. Chandrabhas Narayana, Dr. T. K. Maji, Dr. Eswaramoorthy, Prof. K. S. Narayan, Prof. S. K. Pati, Prof. U. V. Waghmare, Dr. S. Narasimhan, Dr. N. S. Vidhyadhiraja, Prof. S. Ranganathan (Materials Engineering, IISc) and Dr. Ranjan Datta for their valuable courses.

I thank all my batchmates of Int. Ph.D 2008 for their support during my MS programme.

PREFACE

This thesis consists of 3 chapters describing the study of ZnO semiconductor nanocrystals with high resolution electron energy loss spectroscopy (HR-EELS) ina FEI TITAN^{3TM} 80-300 kV transmission electron microscope.

Chapter 1 describes a brief introduction to ZnO semiconductor, its device application, native point defects and defect properties. It also gives a short introduction the technique – High resolution electron energy loss spectroscopy.

Chapter 2 describes briefly the experimental and simulation techniques used in the presented work. This chapter has 2 sections. 2.1 describes experimental methods and 2.2 describes simulation methods.

Chapter 3 describes high resolution electron energy loss spectroscopy study on ZnO nanocrystals with different oxygen vacancy concentration. HR-EELS experiment was done using a FEI TITAN^{3TM} 80-300kV transmission electron microscope and variation in pre-edge features in the core-ionization edges were observed and was compared with theoretical ELNES calculations done by DFT using WIEN2k code.

Table of Contents

CHAPTER 1

Introduction to ZnO semiconductor

1. Introduction

ZnO is a wide band gap (~ 3.3 eV at room temperature) semiconductor with high exciton binding energy (~ 60meV) [1,2]. ZnO based devices like light emitting diodes (LEDs) and laser diodes (LDs) have been demonstrated [3,4]. Also, ZnO has spintronics applications as TM doped ZnO is a promising system as dilute magnetic semiconductor [22].

ZnO is II-VI semiconductor and it has several advantages over its III-V counterpart GaN. One being, there is no native substrate for GaN. So GaN is grown on foreign substrates like sapphire which is 16% lattice mismatched and results in extended defects (10^6 to 10^9 cm^{-3})[5]. But ZnO can be grown on native substrates to reduce the defects very much [6]. Bulk single crystals of ZnO can be grown in a variety of techniques such as hydrothermal synthesis, vapour phase transport, pressurized melt down, metal organic chemical vapour deposition (MOCVD), molecular beam epitaxy (MBE), pulsed laser deposition or sputtering. Also, ZnO can be chemically wet etched which is particularly central in device design and fabrication [7]. Moreover, ZnO is less expensive compared to GaN. Due to its high radiation resistance [8-10] it finds space applications. Having the same crystal structure and closely matching lattice parameters ZnO serves as a very good substrate for growing high quality GaN films [11].

Band gap engineering is possible in ZnO by doping with MgO and CdO. MgO blue-shifts while CdO red-shifts the band gap. Although MgO and CdO crystallize in rock-salt structure, it assumes wurtzite structure for moderate doping in ZnO [12].

Even very low concentration of native impurities and defects can alter its electrical and optical properties [13]. Therefore, to have precise control over conductivity of ZnO, understanding the role of native point defects (i.e. vacancies, interstitials, and antisites) and the incorporation of impurities are central. Another trouble is unintentional n-type conductivity. Several groups have tried to p-dope ZnO and have reported with several growth techniques and several group V dopants (N, P, As, Sb, etc.) [6], but ended up getting irreproducible results. So the p-type ZnO is still elusive in the field of material science. So a clear understanding of the physics is yet to be done. The origin of the *n*-type background conductivity in undoped ZnO films, whether being due to impurities of some native defect or defects, is still under some degree of debate. Some reports assign the residual background to intrinsic defects such as oxygen vacancies (V_O) and interstitial zinc atoms (Zn_i), [14-16] and others to uncontrollable hydrogen impurities introduced during growth [17]. Recent state-of-art density functional theory (DFT) [18-20] and by optically detected electron paramagnetic resonance [21] experiments showed that oxygen vacancies cannot be the cause. It has been shown that O vacancies form deep donor states in the band gap which cannot contribute to n-type conductivity [19]. The well-known green band in ZnO luminescence spectra (a broad peak around 500–530 nm), observed nearly in all samples regardless of growth conditions, is related to singly ionized oxygen vacancies by some and to residual copper impurities by others. But a complete picture is still lacking [6].

Another property of ZnO is its application as transparent semiconductor. No protective covering is needed to stop light exposure since ZnO, being a high band gap material, is

insensitive to visible light. By controlling the conductivity from insulator through n-type to metal facilitates its use as transparent electrodes in flat-panel displays and solar cells [6].

Also, ZnO is a potential spintronics candidate. When a magnetic ion is doped to substitute the cation in a transition metal oxide semiconductor in low concentrations, then the material is called a dilute magnetic oxide (DMO). Diet et al. in 2000, by using the Zener model of carrier mediated exchange, predicted that 5% Mn-doped ZnO with carrier concentration more than 3.5×10^{20} holes/cm^3 has curie temperature >300K [22].

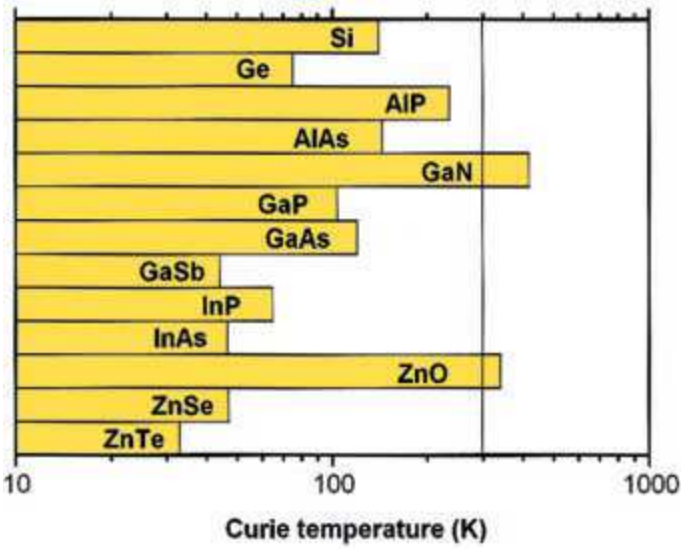

Figure 1: Dietl et al.'s prediction of Curie temperature for various p-type semiconductor containing 5% Mn with carrier concentration of 3.5×10^{20} holes/cm^3. (*Ref. 22*)

This fuelled a lot of effort in the theoretical understanding of ZnO doped with Mn and other transition metal impurities. It can be generalized from most of the publications that, unless charge carriers or point defects are added, the intrinsic ferromagnetism does not occur. These theoretical predictions fuelled a lot of efforts in experiments which claimed observations of ferromagnetism at and above room temperature. But despite many efforts over the last 10 years, a working ferromagnetic DMS device structure at room temperature is yet to be established [23]. The mechanisms for DMS behaviour can be of 2 types, carrier mediated exchange mechanisms and defect based bound magnetic polarons [24]. In carrier mediated

exchange mechanism local magnetic moments interact via free carriers. In this mechanism, more the carrier concentration, better the ferromagnetism. But some experiments suggested direct correlation between ferromagnetism and Zn_i (V_o) [Zn interstitials and O vacancies]. In this case, the higher the number of these defects, better the ferromagnetic ordering. [24]

1.1 Crystal structure

ZnO is II-VI binary compound semiconductor who's bonding nature lies in the borderline between covalent and ionic. Zn and O atom can form covalent bonds with sp^3 hybridization where each Zn atom is in tetrahedral co-ordination with 4 O atom and vice-versa. This results in either hexagonal wurtzite or cubic zinc blende structure. Also, due to substantial ionic character of the bonds one more crystal structure is possible and that is the rock salt structure. Still, the thermodynamically stable phase is wurtzite at ambient conditions [6]. All the three structures are shown in Figure 2.

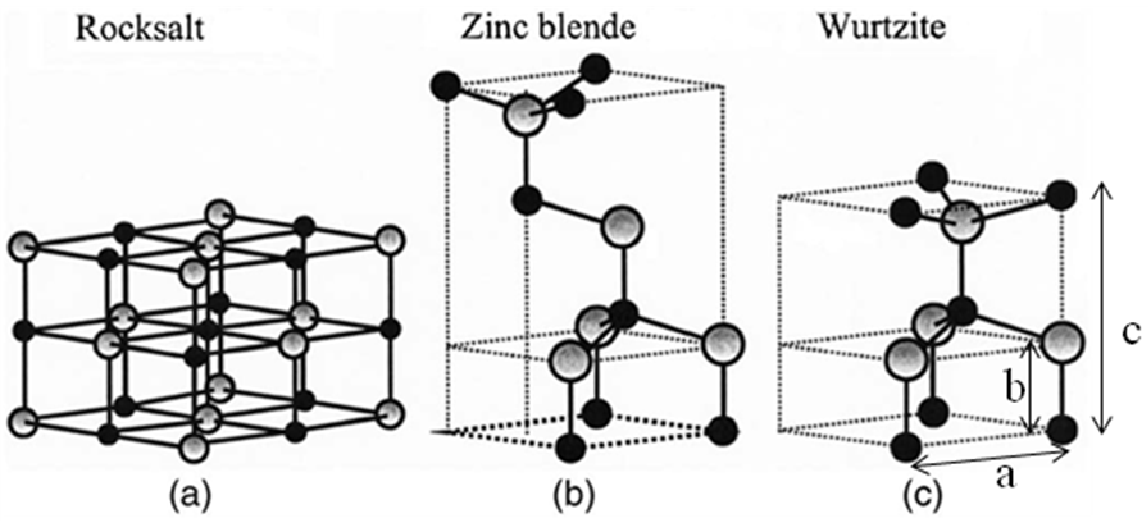

Figure 2: The Rocksalt , Zinc blende and Wurtzite structure of ZnO. In Wurtzite structure, the u parameter is the ratio between b and c. ***(Ref.16)***

The lattice parameter 'a' for wurtzitic structure ranged from 3.2475 Å to 3.2501 Å and 'c' parameter ranged from 5.2042 Å to 5.2075 Å in various experiments. The 'u' parameter (The

ratio b/c) was found to be in the range 0.383 to 0.3856 [6].The space group of Wurtzitic ZnO is $P6_3mc$.

1.2. Native Point defects in ZnO

Native or intrinsic defects are imperfections in the crystal involving only its elements. Examples of native point defects in ZnO are O and Zn vacancies (V_O and V_{Zn}), O and Zn interstetials (O_i and Zn_i), and O and Zn antisites (An O atom placed at the lattice site of Zn atom (O_{Zn}) and vice versa (Zn_O)). Native point defects can strongly affect the optical properties, doping, minority carrier lifetime and luminescence efficiency and magnetism.

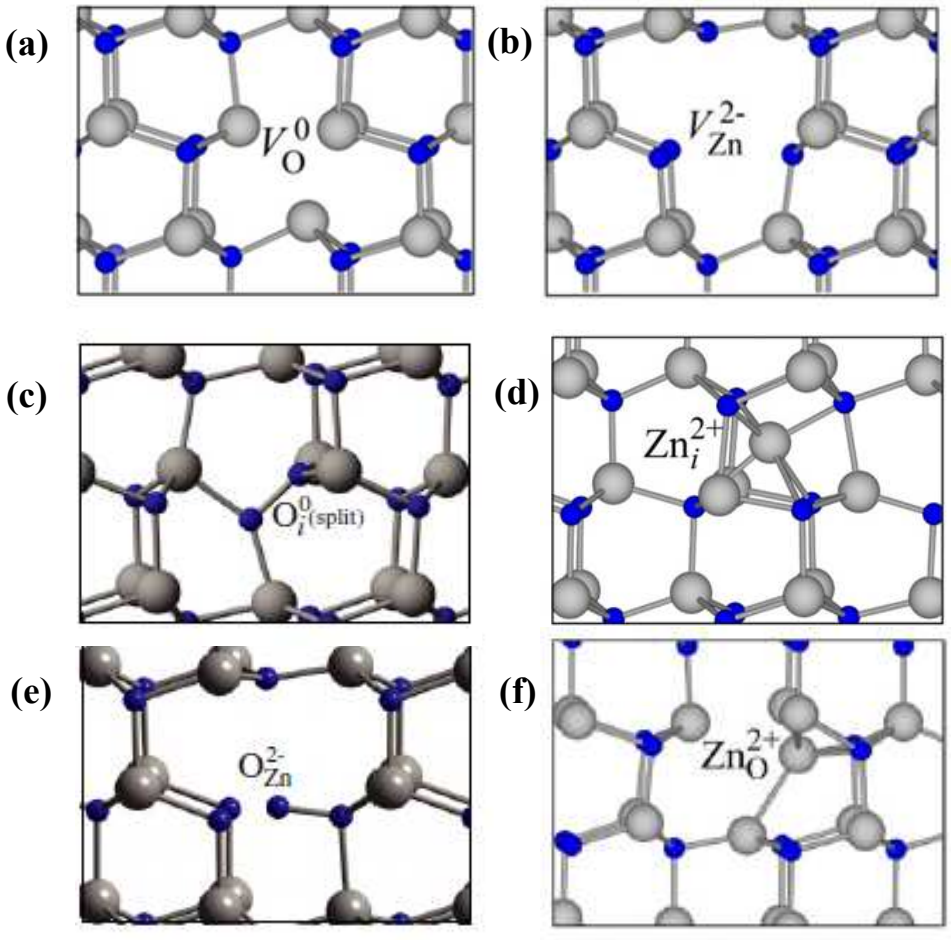

Figure 3: (a) The relaxed structure of (a) neutral O vacancies, (b) Zn vacancies in -2 charged state, (c) neutral O interstitials (d) Zn interstitials in +2 state (e) oxygen antisites in -2 state and (f) Zn antisites in +2 state (*Ref. 61*)

Oxygen vacancies: The electronic structure of oxygen defects can be explained using a simple model within molecular orbital theory. An oxygen vacancy (V_O) involves four sp^3 hybridized Zn dangling bonds and two electrons. These dangling bonds combine to give one fully symmetric, completely filled a_1 state in the band gap and three empty states in the conduction band. The oxygen vacancy can ionize by removing electrons from the filled a_1 state. So 3 charged states are possible. They are 0, +1, and +2. [12]

Zinc vacancies (V_{Zn}): When a Zn atom is removed from the ZnO lattice, the four O dangling bonds carrying a total of 6 electrons hibridize to give a fully occupied symmetric a_1 state located deep in the valence band and three states in the band gap partially occupied with four electrons and therefore can accept at most two more electrons. Thus V_{Zn} is an acceptor defect with 3 possible charge states, 0, -1 and -2. [12]

Oxygen interstitials(O_i): They can exist either as electrically inactive split interstitials (O_i - (split)) configuration or as deep acceptors at the octahedral site (O_i). DFT calculations have shown that when an O atom is placed in a tetrahedral void, it relaxes to give what is known as a split interstitial in which an extra oxygen atom shares the lattice position of one of the oxygen atoms. At this position the oxygen is electrically inactive. O_i(oct) introduces states near the valence band maximum in the band gap and these states are derived from O p states. They can exist in 3 charge states 0, -1 and -2. [12]

Zinc interstitials (Zn_i): The thermodynamically more stable Zn_i is in octahedral configuration when compared to tetrahedral configuration. The interstitial Zn 4s electrons can be transferred into the conduction band and Zn_i acts as donors. They can exist in 0, +1 and +2 charge states. [12]

Zinc and oxygen antisites (Zn_O and O_{Zn}, respectivley): Zn antisite is a double donor, with possible donor states +1, +2, +3 and +4. This can be considered as in combination of defects, $Zn_i + V_O$. Oxygen antisites are acceptor defects, a combination of O_i and V_{Zn}. [12]

1.2.1. Defect concentrations and formation energies

The concentration of point defects in a solid (number of defects / unit volume), assuming thermal equilibrium and neglecting defect-defect interactions, is given by [12]

$$c = N_{site}\, e^{\frac{-E^f}{k_B T}} \qquad (1.2)$$

Where N_{site} is the number of sites per unit volume the particular defect can be incorporated in.

E^f is the formation energy

k_B is the Boltzmann constant

T is the temperature

The formation energy of a point defect D is given by, [12]

$$E^f(D^q) = E_{tot}(D^q) - E_{tot}(ZnO) + n_{Zn}\mu_{Zn} + n_O\mu_O + q(E_f + E_{vbm}) \qquad (1.3)$$

where $E^f(V_O^q)$ is the formation energy of the oxygen vacancy of charge q, $E_{tot}(V_O^q)$ is the total energy of the crystal with vacancy, $E_{tot}(ZnO)$ is the total energy of the pure ZnO crystal, μ_O and μ_{Zn} are the oxygen and Zn chemical potentials respectively, , n_O and n_{Zn} are the number of O and Zn defects respectively, E_f is the Fermi level and E_{vbm} is the energy of the valence band maximum. [12]

$E_{tot}(D^q)$ and $E_{tot}(ZnO)$ can be calculated using electronic ground state energy calculations, for example DFT. Under thermodynamic equilibrium, it is possible to place bounds on the chemical potentials. Under extreme Zn-rich condition (this can be experimentally established by performing the experiment in vacuum or in a chamber filled with Zn vapour), μ_{Zn} (max) $=E_{tot}(Zn)$, and $\mu_O(min) = ½ E_{tot}(O_2) + \Delta H_f(ZnO)$, where $\Delta H_f(ZnO)$ is the formation enthalpy of ZnO. Under extreme O-rich condition (this can be experimentally established by performing the experiment in an oxygen atmosphere), $\mu_O\ (max) = ½ E_{tot}(O_2)$, and $\mu_{Zn}(min) = E_{tot}(Zn) + \Delta H_f(ZnO)$. Here $E_{tot}(O_2)$ and $E_{tot}(Zn)$ can be calculated by using DFT or other electronic ground state energy calculation techniques. E_{vbm} can also be determined by using DFT. The only variable left is E_f, the Fermi level. It is not an independent variable. But if it is taken as an independent variable, it is possible to study the charge state and formation energy of defects as a function of doping level. [12]

A transition level is defined as the Fermi level for which the formation energies of two charged states coincide or in other words, The transition level $\varepsilon(q/q')$ is defined as the Fermi-level position for which the formation energies of charge states *q and q'* are equal. If a transition level is positioned such that the defect can be thermally ionized at room temperature, then it is called a shallow transition level or otherwise it is a deep transition level. [12]

Several groups have done density functional theory (DFT) calculations for native point defects in ZnO [27, 59]. But these calculations are inaccurate since band gap in ZnO is underestimated in both local density approximation (LDA) and generalized gradient approximation (GGA). Different other approaches like self interaction correction, LDA+U, B3LYP, HSE hybrid functional etc. have improved the accuracy [29, 60-61]. Most of the calculations have showed that oxygen vacancies and zinc interstitials have the lowest formation energy followed by Zn vacancies and O interstitials. Oxygen interstitials and

antisites have the highest formation energy. The defects formed under Zn rich condition (V_O, Zn_i and Zn_O) are donors and that formed in O rich condition (V_{Zn}, O_i and O_{Zn}) are acceptors. [22] The results of Janotti et al. [12] are given below.

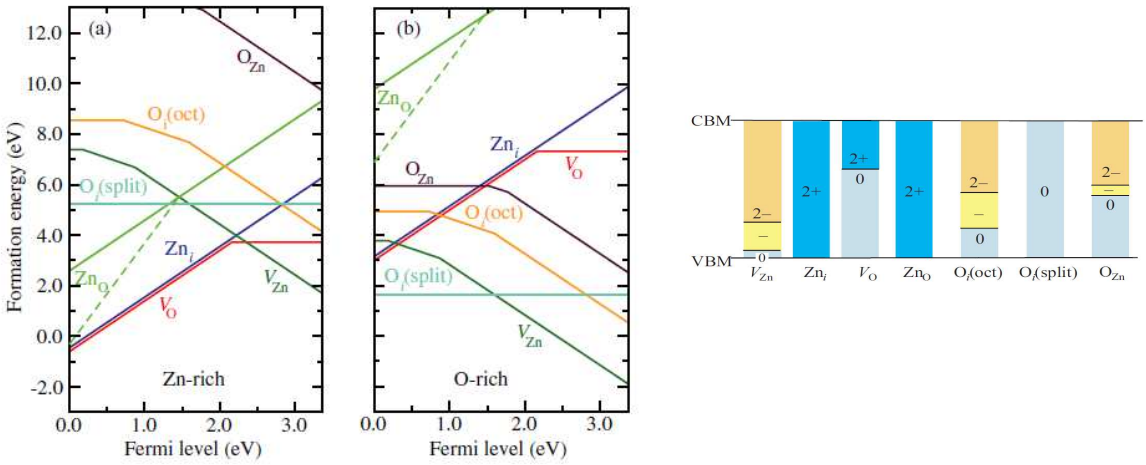

Figure 4: The formation energies of different native point defects in ZnO as per Janotti et al.'s results (a) in Zn-rich and (b) in O-rich condtions. (c) The transition levels in the band gap showing that V_{Zn}, O_i and O_{Zn} are deep acceptors, V_O is a deep donor while Zn_i and Zn_O are shallow donors(*Ref.61*)

A Janotti and C. G. Van de Walle in 2009 reviewed [12] all their calculations on ZnO formation energy and migration energy barrier using state-of-art DFT approach. Their main conclusions are listed below.

- *Oxygen vacancies:* They are deep donors with the transition level $\varepsilon(2+/0)$ at ~1eV below the conduction band maximum (CBM), in the band gap. V_O^{1+} was found not to be thermodynamically stable. The formation energy values are low under Zn-rich conditions and when the Fermi level is near the valence band (p-type material). The vacancy is in V_O^{2+} state in p-type material. In n-type material they have high formation energy and are in V_O^0 state. The migration energy barrier (This is the energy required for a defect to perform self-diffusion) was found to be 2.4 eV for

neutral oxygen vacancy (V_O^0) and 1.7 for V_O^{2+}. These energy values indicated that V_O^0 becomes mobile above temperatures 900 K and V_O^{2+} becomes mobile after 650K.

- *Zinc vacancies:* They are deep acceptors with the transition level *ε(0/1-)* at 0.18 eV and *ε(1-/2-)* at 0.87 eV above the valence band maximum (CBM) .The formation energy values are low under O-rich conditions when the Fermi level is near the conduction band (n-type material) and the vacancy is in V_{Zn}^{2-} state. In p-type material they have high formation energy and are in V_O^0 and V_O^{1-} states. The migration energy barrier (This is the energy required for a defect to perform self-diffusion) was found to be 2.4eV for neutral oxygen vacancy (V_{Zn}^{2-}) and 1.4 for V_{Zn}^{2-}. These energy values indicated V_{Zn}^{2-} becomes mobile after 540 K.
- *Oxygen interstitials:* They have high formation energies. O_i(split) is electrically inactive. O_i(oct) can exist in 3 charge states with transition energies *ε(0/1-)* and *ε(1-/2-)* at 0.72 eV and 1.59 eV respectively. Migration barrier is 1.1 eV. Oi(split) becomes mobile at temperatures above 340 K and O_i(oct) will become mobile at temperatures above 440 K
- *Zinc interstitials:* They are shallow donors and also fast diffusers so are unlikely to be stable as isolated point defects. They will diffuse with a migration barrier as low as 0.57eV.
- *Oxygen antisites:* They have the highest formation energy among the acceptor type native point defects. They are deep acceptors. The antisite oxygen shows high off axis displacements in which the oxygen atom bonds with only one O nearest neighbour.
- *Zinc antisites:* They are shallow donors, but have high formation energies in n-type samples. Have large off-axis displacement and induce large lattice relaxation.

The migration barriers of all these point defects are modest. So sample damage like radiation damage can be healed by annealing at low temperatures. So during epitaxial growth, the point

defects will be in constant migration, so the growth condition can be considered to be near equilibrium.

The positions of the transition energies in the band gap are generally very consistent throughout different publications [12,25,26]. But Oba et al [25] and Vidya et al[26] calculated less formation energy for oxygen vacancies with V_O^0 having ~ 1eV of E^f.

Vidya et al. [26] calculated formation energies of different vacancy complexes. (Vacancy complexes are combination of two or more of the defect types mentioned above). It has been found that all of them have too high formation energies to be feasible at room temperature under thermodynamic equilibrium.

1.2.2. Properties affected by point defects

The three main properties that are affected by point defects in ZnO are conductivity, luminescence and magnetism.

As already mentioned, one of the debated issues in ZnO is the background n-type conductivity. The different calculations done by various groups have unanimously proved that none of the point defects or their complexes could explain this behaviour. V_O has low formation energy in the p-type region and it acts as a donor and thus compensates the p-type conductivity. In the n-type region V_O has very high formation energy and the neutral state is stable. So V_O can only act as compensation centre in p-type material but never can cause n-type conductivity. Similarly, V_{Zn} has very low formation energy in n-type ZnO and the acceptor state is more stable. So, V_{Zn} are compensation centres in a n-type material, but never found to be causing n-type conductivity. In the same way, all acceptor defects and complexes compensate for n-type conductivity and donor defects act as compensation centres for p-conductivity. [12]

ZnO often exhibits weak and broad green luminescence. Janotti et al's calculations show that the cause of green luminescence in ZnO is due to V_{Zn}. When an electron in the conduction band recombines with a hole in the *ε(1-/2-)* transition level at 0.87 eV above the valence band maximum would give rise to luminescence around 2.5 eV. Hofmann et al. Suggested V_O to be responsible for green luminescence based on photoluminescence (PL) and optically detected electron paramagnetic resonance (ODEPR). He suggested a donor level 530 meV below the conduction band which was assigned to the ε(2+/0) of the oxygen vacancy to be responsible for the phenomena. The 2.45 eV emission band is related to a transition from a triplet (S = 1) excited state to the singlet ground state of the neutral oxygen vacancy. [12]

In dilute magnetic semiconductors, some experiments showed direct correlation between ferromagnetism and Zn_i and V_O. In bound magnetic polaron model, an electron is trapped at a particular defect is confined to hydrogenic orbitals with characteristic Bohr radius. When hydrogenic orbitals with sufficiently large Bohr radii overlap with a magnetic cation, super coupling results in bound magnetic polarons (BMPs). The hydrogenic orbital Bohr radii can be sufficiently large for overlapping between neighbouring BMPs resulting in ferromagnetic ordering. [24]

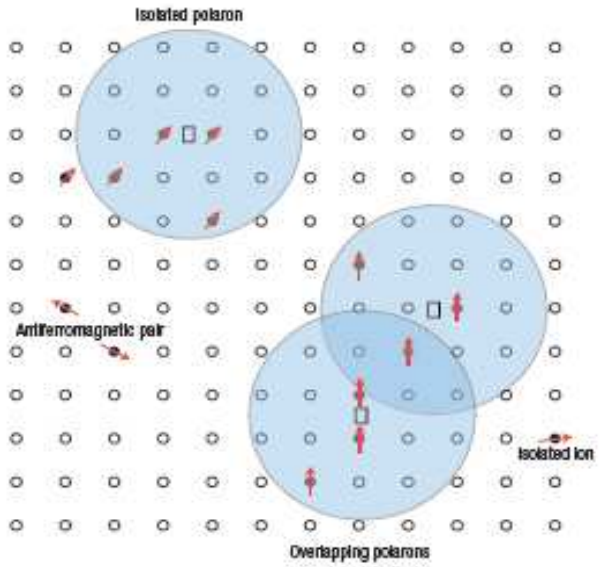

Figure 5: The schematic illustration of the BMP model. Cation sites are represented by small circles. The oxygen vacancy sites are represented by small rectangles. The arrowed black circles are magnetic ions with arrows show the direction of the direction of magnetic moment. (*Ref. 24*)

1.3. High resolution electron energy loss spectroscopy

High spatial and energy resolution is required for advanced imaging, diffraction and spectroscopic study of the atomic scale processes [27]. Transmission electron microscope (TEM) is of great value since it has high lateral resolution to give excellent structural information via high resolution imaging and electron diffraction. Recent developments in TEM which is equipped with electron energy loss spectrometers (EELS) have established an absorption spectroscopy of the highest spatial resolution and measurable intensity even from sub-nanometer sized materials [28].

EELS maps the available states in a solid state compound above the Fermi level of the excited atom. In EELS technique high energy electron beam (100 – 1000 keV) is passed through samples of thickness (10-100 nm) and the energy distribution of the transmitted electrons is recorded. The ionization edges map the conduction band of the excited atom which gives chemical and solid-state information.

For thermionic sources the gun is the limiting factor for resolution. For tungsten the ultimate resolution is ~ 3eV and for LaB_6 is will be ~1.5 eV. So EELS ideally requires that you have a field emission gun (FEG). Conventional TEM/EELS gives a best energy resolution of 0.6 eV with a FEG. Instead of even this resolution this may result in a loss of invaluable information from the EEL spectra. With the introduction of TEM/EELS with some latest commercially available monochromators for EELS, the energy resolution can be as good as < 0.1 eV. Basically, a monochromator is an EELS system fitted on the FEG source and the selecting slit refines the already narrow energy spread of the FEG additionally giving extremely fine details in the spectra. The monochromators have perpendicular electrostatic and magnetic fields which permit the chosen electrons to travel in a straight line in the TEM column.

Monochromated valence EELS (or VEELS) or core-loss spectroscopy, for its high resolution, opens up new opportunities to study band gap and other optical properties. A gun monochromators facilitates this in 2 ways.

1. It reduces the width of the zero loss peak
2. It makes the zero loss peak more symmetric.

With these advances, the zero loss peak no more extends to the band gap region allowing one to study even narrow band gap materials. The energy region in the band gap is difficult to study using optical methods because it cannot give momentum information. EELS can give peaks corresponding to both direct and indirect gaps.

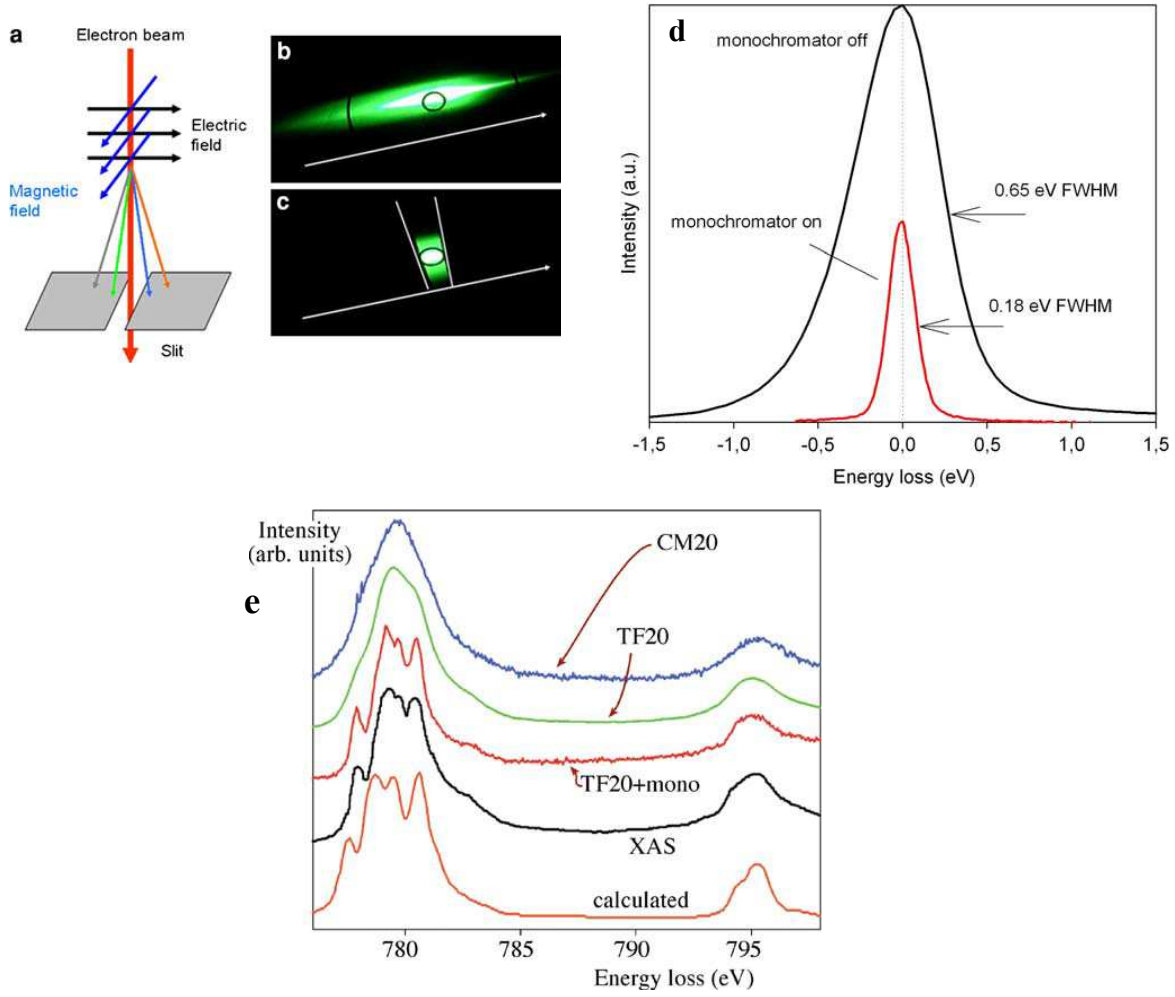

Figure 6: (a) Schematic diagram of the monochromization using a wien filter. Dispersed electron beam on the viewing screen (b) before and (c) after introduction of energy selecting slit. (d) Comparison of zero loss peak with monochromators off and a wien type monochromator on in the accelerating mode.(*Ref. 66*). (e) Comparison of Co L2,3 spectra from: a Philips CM20 thermionic source, an FEI Tecnai TF20 with a cold FEG, a TF20 with a monochromator, a synchrotron (X-ray absorption spectrum), and a calculated spectrum using crystal-field theory. The improvement in resolution with monochromation is clear. (*Ref. 30*)

1.3.1. HREELS to study ZnO

Grogger et al. [29] studied the band gap region of a single ZnO nanorod with a monochromated Tecnai F20 microscope. With an STEM probe of diameter ~ 4nm yielding about 0.2 nA current and energy resolution of 0.2 eV, the spectra were acquired. The spectrum recorded at the centre of the nanorod accurately measured the band gap. Unless monochromator was used, the band gap could have been buried under the zero loss peak.

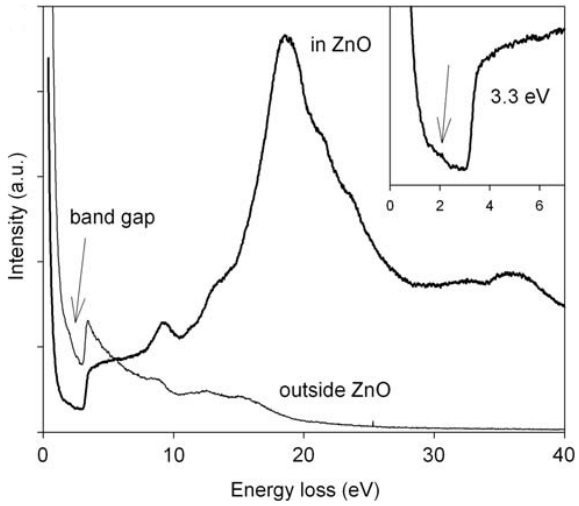

Figure 7: The low loss region of the EELS spectra recorded with beam falling inside and outside the ZnO nanorod. Inset shows the band gap region which has few Cerenkov peaks. (*Ref. 29*)

The electron beam can also polarize and excite the surface electronic modes. From this the dielectric function can be calculated. The main peak at 18 eV (Figure 7) can be attributed to a bulk Plasmon excitation (at 9.5 eV, 13.5 eV, 21.5 eV and 23eV) are interband transitions from valence band to the empty states of the conduction band.

1.3.2. Energy loss near edge spectra (ELNES)

The electron energy loss spectra consists of atomic absorption resulting in the loss of incident beam energy from zero (elastic scattering) to several thousands of eVs (inelastic scattering). In the low loss region, the spectra is dominated by collective excitons (plasmons). The edge threshold and the structures which start from the edge onset and extend to 30-40 eV are called near edge structures (ELNES). ELNES have strong modulations and gives information on inter atomic distances, bonding and co-ordination.

Theoretical background

If fast moving electrons are treated as plane waves, and the electrons are scattered into a solid angle dΩ and an energy range dE the absorption intensity is described by double differential cross section given by [71]

$$\frac{d^2I}{dEd\Omega} = \frac{4\Upsilon^2}{a_0^2}\left|\frac{\langle f|\exp(i(q.r))|i\rangle}{q^2}\right|^2 \qquad (1.4)$$

Where a_0 is the Bohr radius, Υ is the relativistic correction factor q is the scattering wave vector ($q= k_f - k_i$ where k_f is the final wave vector and k_i is the initial wave vector), r is the co-ordinate of the absorbing atom, i and f are the initial and final states. If $q.r \ll 1$ then dipole selection rule applies and only those transitions are allowed in which $\Delta l = \pm 1$, where l is the angular momentum quantum number. If an average is taken ,over all the direction of the scattering wave vector, the R.H.S of the equation 1.4 is separable into atomic like matrix elements, m_L, those vary slowly with energy and angular momentum resolved density of states ρ_L and can be written as equation 1.5. [71]

$$\frac{d^2I}{dEd\Omega} = \frac{4\Upsilon^2}{a_0^2}\left[|m_{L+1}|^2\rho_{L+1}(E) + |m_{L-1}|^2\rho_{L-1}(E)\right] \qquad (1.5)$$

1.3.2.1 ELNES study on defectless ZnO

The Zn L_3 occurs at ~ 1020 eV energy loss. The Zn L_3 corresponds to electronic transitions from Zn $2p_{3/2}$ to Zn 3d and 4s states hybridized with O 2p states [31]. The appearance of four peaks (namely A, T, E, TT, see Figure 8) in Zn L_3 ELNES of w-ZnO was explained by point group symmetry in the first co-ordination unit. $(ZnO4)^{6-}$ was taken to be in tetrahedral

symmetry (T_d) and under this condition Zn 4s gave rise to a_1, Zn 4d gave rise to t_2 and e molecular orbital respectively. 4p became t_2. Zn 4d and 4p hybridizes to form two t_2.

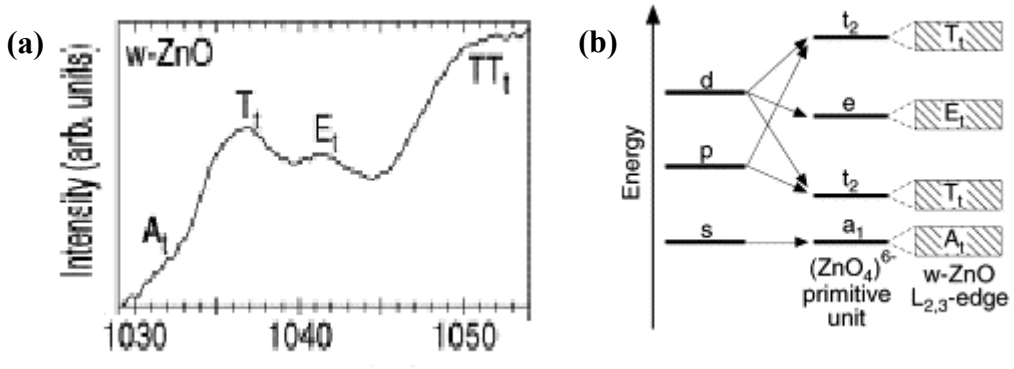

Figure 8

: (a) Zn $L_{2,3}$ edge of w-ZnO (b) Schematic diagram showing the origin of 4 peaks in Zn $L_{2,3}$ edge.(*Ref. 67*)

The O K absorption threshold occurs at ~ 530 eV energy loss. The O K absorption edge of bulk ZnO can be explained by the transition from O 1s to O 2p unoccupied levels [32]. O 2p states hybridize with Zn 4s states to give ELNES in the energy range ~ 530 to 539 eV. From 539 to ~ 550 eV, the main contribution is from O-2p states hybridized with Zn-p states. Above 550 eV is the transition to O2p-Zn4d hybridized levels.

CHAPTER 2

HREELS – Experimentation and Simulation

2.1 Experimental EELS

2.1.1. EELS instrumentation

The electron energy loss spectrum is recorded in a TEM using a Gatan parallel EELS (PEELS) spectrometer. It involves a magnetic prism spectrometer and it is advantageous over an electrostatic or combined magnetic/electrostatic spectrometer for several reasons

- It is compact and easily interfaced to the TEM.
- It offers sufficient energy resolution to distinguish spectra from all the elements in the periodic table and so is ideal for analysis.
- Electrons in the energy range 100–400 keV, typical of AEMs, can be dispersed sufficiently to detect the spectrum electronically, without limiting the energy resolution. [30]

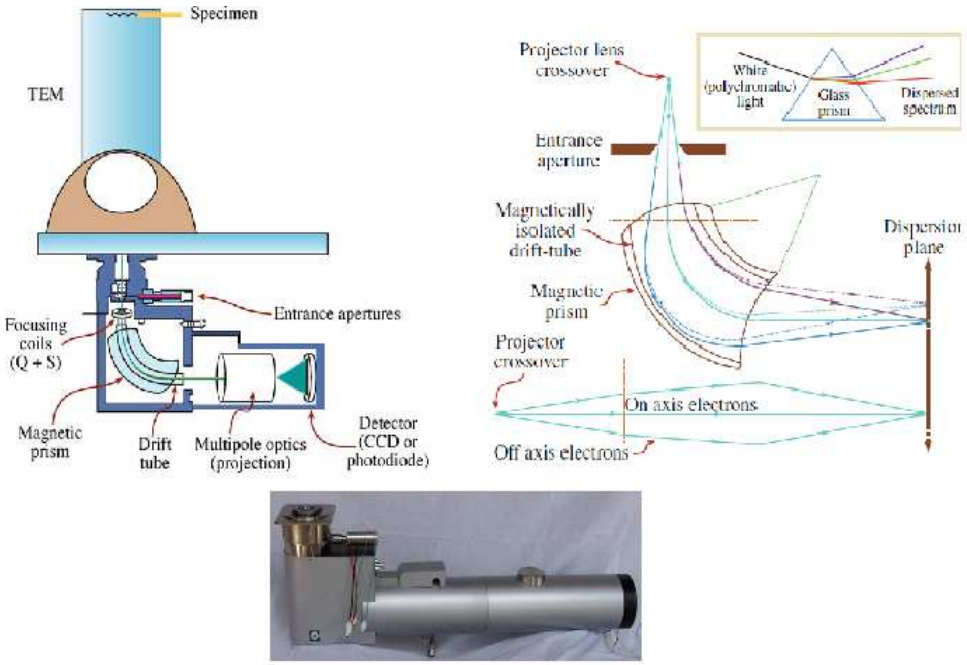

Figure 1: (a) The schematic of PEELS fitted below the viewing screen. (b) Functioning of magnetic prism for dispersion of electrons of different energies represented schematically. Analogy with dispersion of white light also shown (c) The GATAN PEELS. (*Ref. 30*)

2.1.2 Modes of EELS operation in a TEM

2.1.2.1.TEM image mode

In the TEM image mode an image will be present at the viewing screen of the microscope and a diffraction pattern (DP) is present at the back focal plane of the projector lens which serves as the object for the spectrometer. So a diffraction pattern is focused at the spectrometer.

2.1.2.2. TEM diffraction mode

In TEM diffraction mode a diffraction pattern is present at the viewing screen. The image will be present at the back focal plane of the projector lens which serves as the object for the spectrometer.

2.1.3. Parameters involved in an EELS experiment

2.1.3.1. Dispersion

The dispersion in an EELS spectrometer varies with energy of the electron beam and the strength of the magnetic prism. For example, consider a GATAN spectrometer working on a TEM with 100 keV electrons, the dispersion will be ~ 2μm/eV. This is too low a dispersion therefore the quadrapole lenses are used to magnify to ~ 15 ×.

2.1.3.2. Resolution

The resolution of an EELS spectrometer is defined as the full width at half if the maximum of the primary electrons (zero loss peak). For thermionic sources the gun is the limiting factor for resolution. For tungsten the ultimate resolution is ~ 3eV and for LaB_6 is will be ~1.5 eV. So in order to increase the resolution, a field emission gun (FEG) becomes necessary. Conventional TEM/EELS gives a best energy resolution of 0.6 eV with a FEG. But even this energy resolution results in a loss of valuable information from the EEL spectra. With the introduction of TEM/EELS with some latest commercially available monochromators for EELS, the energy resolution can be as good as < 0.2 eV.

2.1.3.3. Point spread function

Point spread function refers to a ‘delocalization’ in the spectrum. For example, a particular structure, say zero loss peak, if the spectrum is expected to come at one channel of the CCD, still some part of it can ‘spread’ to its neighbouring channels as shown in Figure 2.

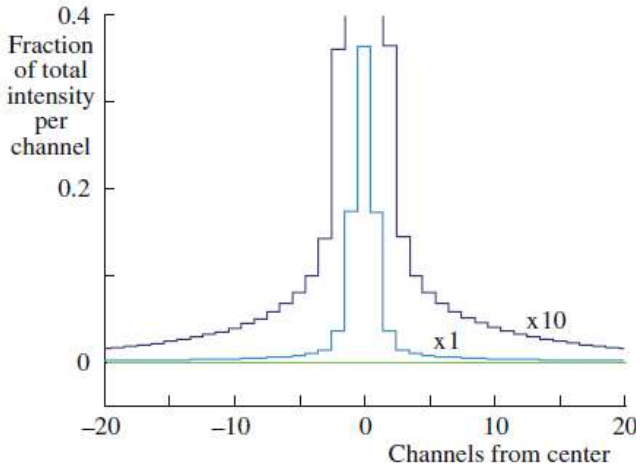

Figure 2: The point spread function demonstrated for the zero loss peak (*Ref .30*)

2.1.3.4. Spectrometer collection semi angle β

It is defined as the half of the angle the collection aperture at the specimen.

In the TEM mode, without inserting the objective aperture, β is nearly 100 mrad and when objective aperture is inserted, the collection semiangle is[30]

$$\beta = \frac{\beta_{ob}}{M} \qquad (2.1)$$

Where β_{ob} is the aperture semi-angle at the objective lens and M is the magnification.

In the diffraction mode, if the camera length l is known the collection semi-angle β is, [30]

$$\beta = \frac{D}{D_A}\frac{d}{l} \qquad (2.2)$$

Where D is the distance from the projector cross-over to the recording plane

D_A is the distance between the crossover and the entrance aperture

d is the diameter of the enrance aperture

l is the camera length.

2.1.3.5. Spatial resolution

Spatial resolution in TEM-EELS depends on the mode of operation, i.e. either TEM image or diffraction mode. In the TEM mode, the origin of the signal corresponds to the de-magnified image of the spectrometer aperture in the object plane. For example, consider a magnification and of 100 kx with an aperture of EEL spectrometer 1mm, the diameter of the object area contributing to the spectrum will be about 10 nm. However, at higher energy losses, the chromatic aberration of the objective lens introduces contribution from object regions outside the above mentioned value. In TEM mode the region that contributes to EELS can be limited using a selected area aperture (SAD aperture in the image plane of the intermediate lenses).

TEM mode is appropriate for recording EELS with large β and high resolution but compromising for the spatial resolution. For highest spatial resolution, one has to use TEM-diffraction mode. A focused electron beam on the sample (STEM – scanning TEM) can reduce the area of contribution remarkably. In this mode spectrum can be recorded from each atomic column

2.1.4. Titan^{3TM} 80-300kV TEM

Titan^{3TM}80-300 TEM scanning/transmission electron microscope (S/TEM) with a high tension voltage range of 80- 300 keV. It is factory aligned to 80keV and 300 keV. This microscope is equipped with image and probe corrector so that it can achieve a resolution of 1Å or better and can have energy resolution of better than 0.2 eV. Techniques like high resolution transmission electron microscopy (HRTEM), high resolution scanning transmission electron microscopy (HRSTEM), area selected diffraction, convergent beam

electron diffraction (CBED), EDX analysis, high spatial and energy resolution EELS etc. can be done with this microscope.

Figure 3: Titan^{3TM}80-300 TEM

2.1.5. Procedure of EELS experiment with monochromator in Titan microscope

An area on the TEM grid where there is no amorphous carbon or sample was selected. By using a suitable magnification GIF tuning was done. GIF tuning is mandatory before acquisition of EELS spectra in order to normalize the intensity value of any previously measured data. In our case GIF tuning with an entrance aperture of 1μm was done in order to reduce the beam intensity that will be exposed to the GIF camera. Then the zero loss peak was aligned and the monochromator was excited in steps from 0 to 1.8.

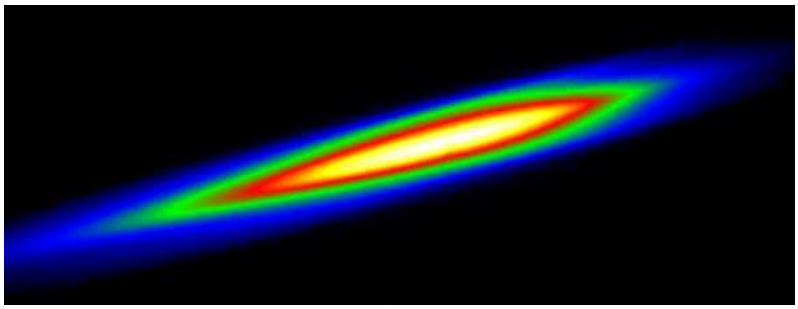

Figure 4: The elongated probe after monochroator excitation.

Then the spectra were acquired and the background due to plural scattering was subtracted using digital micrograph software.

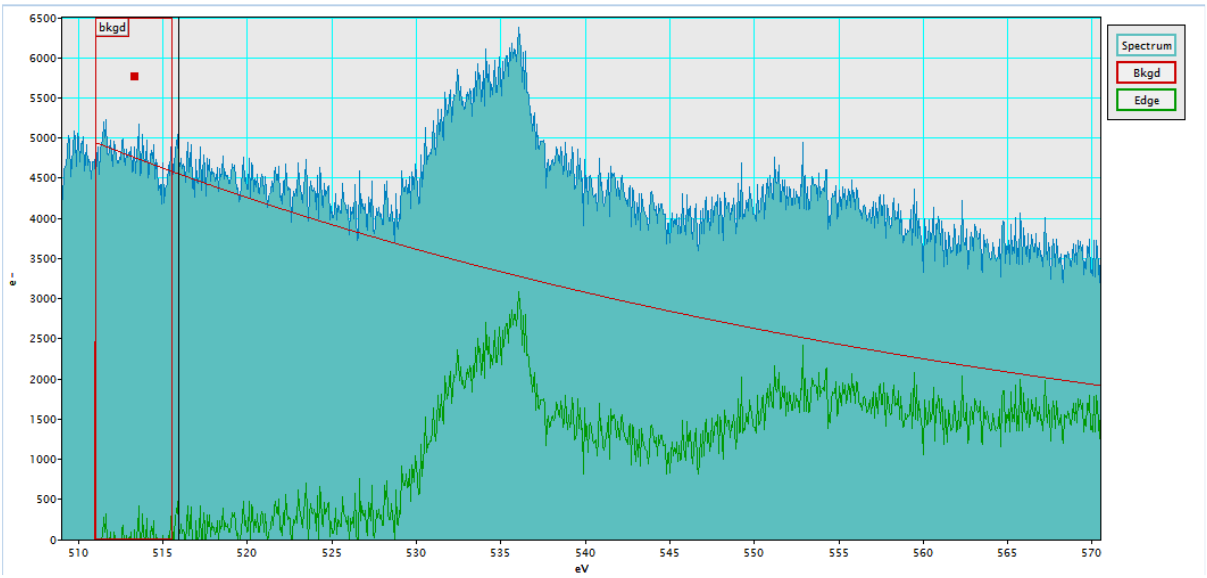

Figure 5: Background subtraction. The plural scattering background is subtracted to obtain the signal (The example given is in the case of O K edge).

Thus obtained signals are then smoothed by using adjacent average method in which 20 adjacent points are averaged.

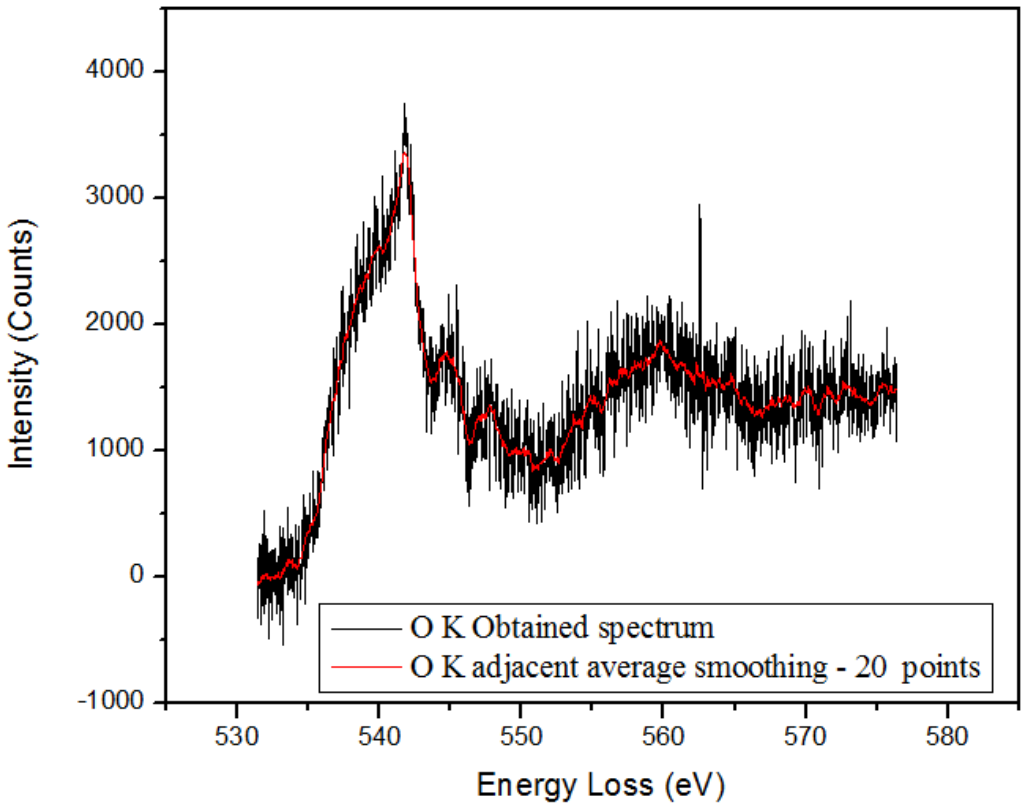

Figure 6: Smoothening of spectrum using 20 point adjacent averaging. This process reduces noise in the spectra.

The derivative of so obtained spectrum also was taken to manifest the fine features in the spectra which were further smoothened by 5 adjacent points averaging.

2.2 EELS simulation

2.2.1. Density functional theory (DFT)

2.2.1.1. The Kohn-Sham equations

While many approaches like Hartree – Fork method solve the Schrödinger equation in terms of wave functions, density functional theory (DFT) deals with electron charge density. This has apparent advantages, like limiting the number of dimensions. For a N-particle system the number of dimentions is 3 for DFT, compared to 3N for a wave function. Density functional

theory limits itself to useful information (the charge density), not the wavefunction which lacks any physical significance. According to DFT, these can be retrieved from the charge density. DFT is based on two theorems known as the Hohenberg-Kohn theorems. The first theorem states that there is a one-to-one correspondence between the ground state electron density $n(r)$ of a many-electron system and the external potential acting on it.[1,2] This is equivalent to the external potential being expressed as a functional of the electron density. The ground state wave function, $\psi(r_1, ..., r_N)$, is a functional of the external potential and, therefore, also of the density. The energy of a system is given by, [40]

$$E = \langle \psi [n(r)] | H | \psi [n(r)] \rangle \qquad (2.3)$$

where H is the Hamiltonian for the system, and so the energy also is a functional of the density. The Hamiltonian can expressed as the sum of the kinetic energy (T), the interaction energy for the electron-electron interactions (U) and the external potential (V), which includes the electron-ion interactions, so that the energy becomes, [40]

$$E[n(r)] = \langle \psi [n(r)] | T + U + V | \psi [n(r)] \rangle \qquad (2.4)$$

The second of the Hohenberg-Kohn theorems states that, for E[n(r)] to be a minimum, the ground state wave function and therefore the ground state density must be used in equation (3). This means that if E[n(r)] is minimized with respect to the density, the ground state density and energy have been obtained.

The Kohn-Sham approach is followed to make this theory work [35]. The essence of this approach is to map the interacting system onto a non-interacting electrons system that has the same total energy and ground-state electron density. Solutions for this non-interacting system can be obtained numerically. This density can be expressed as the sum of independent orbital contributions. [40]

$$n(r) = \sum_{i=0}^{N} \phi_i^* \phi_i \qquad (2.5)$$

The Hamiltonian of this non-interacting system can be written as a sum of several contributions, [40]

$$H = -\frac{\hbar^2 \nabla^2}{2m} + \hat{U}_{ion}(r) + \hat{U}_{coulomb}(r) + \hat{U}_{xc}(r) \qquad (2.6)$$

where the first term is the operator corresponding to the kinetic energy of a system of non-interacting electrons, U_{ion} is the nuclear potential, $U_{Coulomb}$ is the potential corresponding to the Hartree energy (the interaction energy between a single electron and the charge density from all the other electrons) and $U_{xc}(r)$ is known as the exchange-correlation potential. It is formally defined as [8]

$$U_{xc}(r) = \frac{\delta E_{xc}[n(r)]}{\delta n(r)} \qquad (2.7)$$

where $E_{XC}[n(r)]$ is the exchange-correlation energy. This energy is the sum of (i) Exchange energy (E_X - the difference between the real kinetic energy and that of a system of non-interacting electrons) and (ii) the correlation energy (E_C - the difference between the real interaction energy between the electrons and the Hartree energy). Adding correlation and exchange is advantageous because functionals often perform better for the sum than for the separate terms, due to cancellation of errors. A series of single particle equations, known as the Kohn-Sham equations, can now be obtained using the wave functions used to construct the density. [40]

$$H\phi_i(r) = \varepsilon_i \phi_i(r) \qquad (2.8)$$

The exchange correlation potential can be approximated in several ways. The simplest of approaches is to use a functional which depends only on the local density – the Local Density Approximation (LDA) [36, 37] – In this functional, essentially, the system is treated as a homogeneous free electron gas, making it credible that LDA work best for fairly homogenous systems. The LDA is the most often used functional, and although its failures are many, it has been quite successful. Roughly for atoms and molecules, the exchange energy is underestimated by 10%, and the correlation energy is overestimated by a factor of 2 – 3, leading to a total exchange correlation energy underestimated by 7% [38]. LDA gives fairly good charge densities, but less good exchange correlation potentials, which can lead to ionization potentials being unreliable. The results are better for solids, where the correct band structure is found. However, the band gap is underestimated by up to a factor of two. Sometimes, semiconductors are falsely predicted to be metals. Bond lengths tend to be reliable. Lattice parameters are typically underestimated by a few percent. LDA is not the best choice for calculating magnetic properties. It wrongly predicted iron to be non-magnetic at ground state. Normally LDA tends to make systems more homogeneous than they really are. [38]

The generalized gradient approximation (GGA) [39] additionally takes into account the gradient of the charge density, making it a semi-local approach. Although GGA is formally superior to LDA, in practice it doesn't always lead to better results [38]. GGA yields better total energies than LDA (important for structure optimization). The errors in exchange energies and in correlation energies are smaller than in LDA. The artificial over-bonding of s-states relative to p (and p relative to d, etc.) of LDA is much improved in GGA. GGA also treats molecules and atoms on more equal footing. This leads to better binding energies than LDA, better dissociation energies, atomization energies, energy barriers, etc. GGA also gives weaker and less localized bonds than LDA, and as a result, GGA tends to find larger bond

lengths than LDA, which has a tendency to over-bind – but sometimes GGA overcorrects.[6] Lattice parameters are slightly larger than in LDA and tend to be very accurate. GGA is much better at predicting the correct magnetic ground state than LDA, but the magnetic moments can be unrealistically large.

2.2.1.2. Self consistent field

In DFT, the electron density is calculated in cycles and checked for consistency. The flow chart of the programme is given it Figure 7. First step is to construct the basis set required to expand the density functional quantities. A trial electronic density is built as the first guess. This is usually done by using a superposition of atomic-like densities localized on each atomic site present. Then the density functional Hamiltonian is built and solved by diagonalizing and computing the energies, then the basis set coefficients are updated and a new charge density n'(r) is computed. If new charge density is consistent with the previous one, the programme ends, otherwise it enters the loop again

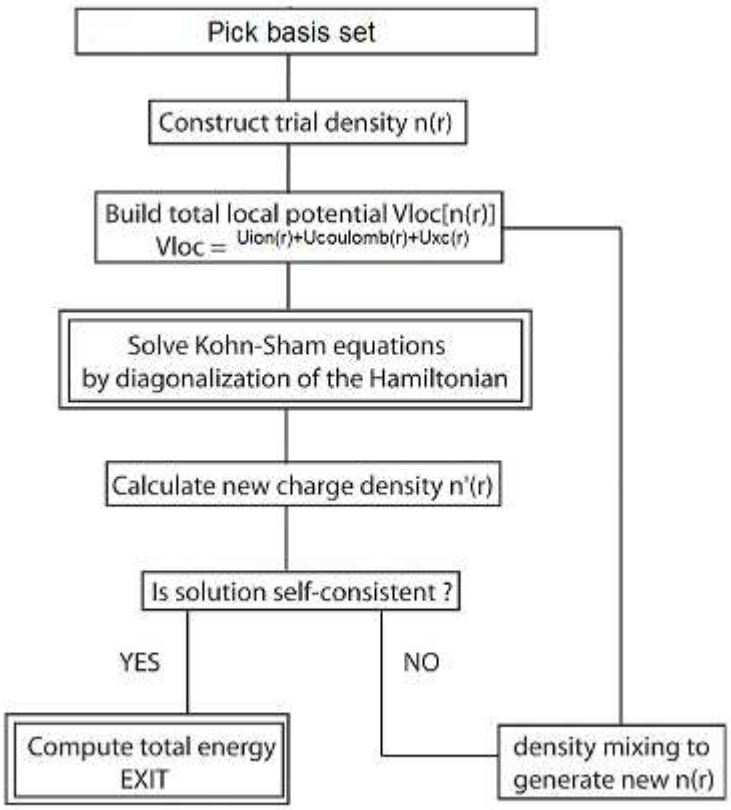

Figure 7: General schematic for self consistent field algorithm.

2.2.1.3. Implementation of DFT in WIEN2k program – The LAPW method

The linearized augmented plane wave (LAPW) method is one of the most accurate methods for electronic structure calculation of crystals. It uses local spin density approximation (LSDA) and generalized gradient approximation (GGA).

LAPW solves Kohn-Sham equation for the ground state energy, eigen values, ground state electron density of a many electron system by using a special basis set which is described below.

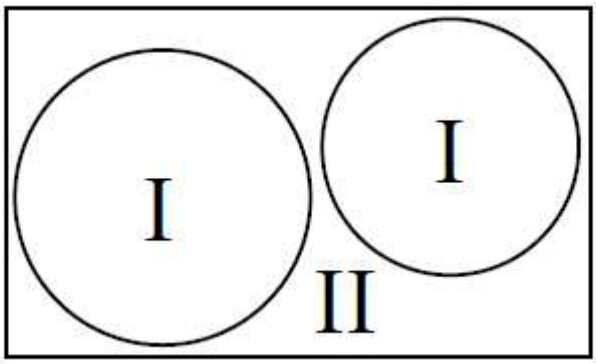

Figure 8: Partitioning of the unit cell into (I) atomic sphere and (II) interstitial regions

The special basis set is achieved by dividing the unit cell into 2 regions. (I)- non-overlapping atomic spheres and (II) interstitial regions. In these two types of regions, different basis sets are used.

1. (I) Inside the atomic sphere t, of radius R_t, a linear combination of radial functions times spherical harmonics $Y_{lm}(r)$ is used.

$$\phi_{k_n} = \sum_{lm}[A_{lm,k_n} u_l(r,E_l) + B_{lm,k_n} \dot{u}_l(r,E_l) Y_{lm}(\hat{r}) \quad \textbf{(2.9)}$$

Where $u_l(r,E_l)$ is the regular solution of the radial schrodinger equation for energyE_l. $\dot{u}_l(r,E_l)$ is the energy derivative of u_l at the same energy. A linear combination of these two functions constitutes the linearization of the radial function. The coefficients $A_{lm}$and $B_{lm}$are functions of k_n ($k_n = k + K_n$, where k is the wave function inside the first Brillouin zone and K_n is the reciprocal lattice vector.

2. (II) In the interstitial region, a plane-wave expansion is used.

$$\phi_{k_n} = \frac{1}{\sqrt{\omega}} e^{ik_n \cdot r} \quad \textbf{(2.10)}$$

The solutions to the Kohn-Sham equations are expanded in the combined basis set of LAPWs according to the linear variation method.

$$\psi_k = \sum_n c_n \phi_{k_n} \quad (2.11)$$

The convergence of the basis set is controlled by a cut-off unit-less parameter $R_{mt}K_{max} = 6-9$, where R_{mt} is the smallest muffin-tin radius in the unit cell and K_{max} is the magnitude of the largest K vector in the equation.

2.2.1.4 Usage of programs in WIEN2k

WIEN2k runs only in a linux operating system which consists of a lot of independent fortran programs linked via C-SHELL scripts. To start a calculation, in the working directory, for example **case**, a master input file, describing the structure, named **case.struct** should be present. Then the calculation can be initiated by using the script **init_lapw** and this consists of initiation of the following programs.

1. NN: a program which calculates the nearest neighbour distances of all the atoms
2. SGROUP: determines the space group of the crystal
3. SYMMETRY: Determines point groups of individual atomic sites, generates the LM expansion for the lattice harmonics, local rotation matrices.
4. LSTART: Generates free atomic densities
5. KGEN: generates k-mesh in the irreducible Brillouin zone.
6. DSTART: Generating the first density for the self consistent field (SCF)cycle to start with.

After initialization, the SCF can be started by running the script run_lapw. This consists of the following auxiliary programs

1. LAPW0: Generates potential from density
2. LAPW1:Calculates valence band eigen values and eigen vectors
3. LAPW2: Calculates valence band densities from eigen vectors
4. LCORE: Calculates core states and densities.
5. MIXER: Mixes input and output densities.

2.2.2. Theoretical ELNES in WIEN2k

The relativistic EELS double differential cross-section is given by

$$\frac{\partial^2\sigma}{\partial\epsilon\partial\Omega} = \left[\frac{4\gamma^2 a_0^{-2}}{q^2-\left(\frac{E}{\hbar c}\right)^2}\right]^2 \frac{k_f}{k_i}\sum_{if}\left|\left\langle f\left|1-\frac{\boldsymbol{v}_0\cdot\boldsymbol{P}}{m_e c^2}\right|i\right\rangle\right|^2 \delta(E_f-E_i-E) \qquad (2.12)$$

This is the basic equation for the TELNES2 program in WIEN2k.The R.H.S of the equation can be separated into atomic like matrix element (m_L) and angular momentum resolved density of states (ρ_L) by rigorous mathematics. The DOS part is contributed by the DFT calculation in WIEN2k and the transition matrix is contributed by TELNES2 itself. [8]

CHAPTER 3

HREELS of ZnO nanocrystals with different oxygen vacancy concentrations [1]

3.1. Summary

High resolution electron energy loss spectroscopy (HR-EELS) was used to characterize the electronic structure of ZnO nanocrytals with different oxygen vacancy concentrations. As synthesized ZnO nanocrystals show very significant green luminescence, the intensity of which decreases as the annealing temperature increases under oxygen atmosphere. The green luminescence significantly quenches at 400°C. O-K and Zn-L_3 pre-edge absorption structures of ZnO nanocrystals were studied by HR-EELS as a function of annealing temperature. More absorption edge peak broadening and more variations in pre-edge absorption edge structure of Zn L_3 were observed in experimental electron energy loss spectroscopy (ELNES) spectra as the oxygen defect concentration increased. All electron density functional theory based (WIEN2k) calculations of electronic density of states (DOS) and electron energy loss near edge structure (ELNES) were carried out with cases of different oxygen vacancy concentrations and compared with experimental spectra. Appearance of additional peaks in pre-edge electron energy loss structure with increasing oxygen vacancy is shown to be due to the oxygen defect states in the band gap of ZnO.

[1] **Electron energy loss spectroscopy of ZnO nanocrystals with different oxygen vacancy concentrations** K. Dileep, L. S. Panchakarla, K. Balasubramanian, U. V. Waghmare, and R. Datta, J. Appl.Phys. 109, 063523 (2011)

3.2. Introduction

A detailed introduction to ZnO semiconductor is already given in chapter 1(sections 1.1.1 to 1.1.4). Chemically synthesized ZnO nanocrystals exhibited broad green emission band besides the expected UV band [41]. The green emission can be attributed to O point defects since the green emission intensity was reducing with increasing annealing temperature under oxygen atmosphere. Green emission is found to be significantly quenched after annealing at 400°C, in O_2 atmosphere. ZnO pre-edge Zn L_3 and O K are studied both experimentally and theoretically using density functional theory (DFT) in the WIEN2k program.

3.3. Background

X-ray absorption spectroscopy technique has been previously studied for the defect structure of ZnO. Hsu et al reported XANES (Zn K absorption edge) of Co doped ZnO annealed under different conditions [42]. ZnO film annealed in oxygen shows increase in *p* orbital DOS (given by the area under the XANES absorption curve) compared with sample annealed under Ar/H_2 condition. Appearance of extra feature at pre edge structure of Zn K absorption edge was attributed to the increase in oxygen vacancy for samples annealed under Ar/H_2 gas and is associated with highest saturation magnetization among samples annealed under different environmental condition.

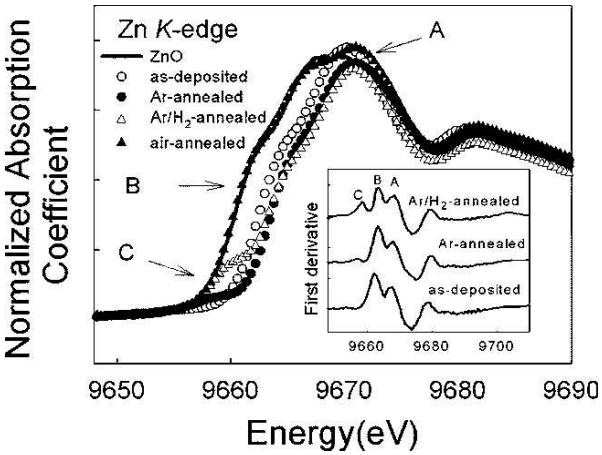

Figure 1: Zn K edge of thin films as deposited and annealed at different atmospheres. The inset shows first derivatives. (*Ref. 42*).

Theoretical calculation in real space based on FEFF 8.2 code also supported the appearance of extra peak in Zn K pre-edge structure corresponding to increasing number of O atom removed from the structure.

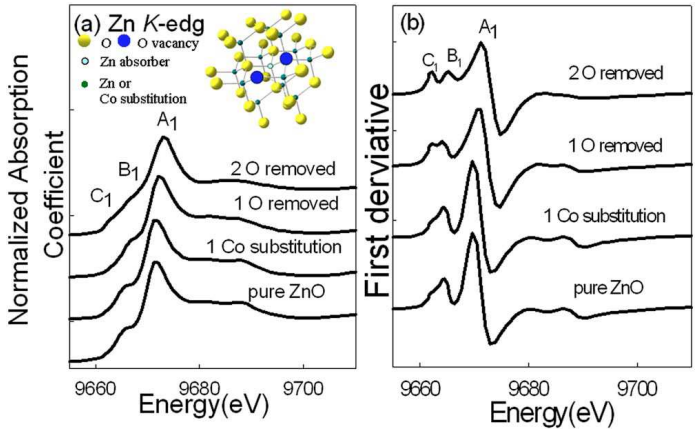

Figure 2: (a) Theoretical Zn K XANES and (b) its first derivative. The emergence of extra peaks at the pre-edge region is observed. (*Ref. 42*).

Muller et al reported that O K edge absorption peak and associated fine structures wash out with increasing amount of oxygen vacancy in SrTiO3 thin film. [43]

The implications of Zn L_3 and O K on the electronic structure of ZnO are already discussed in section 1.6.1.

3.4. Relevance of the presented work

EELS has the advantage over XANES for its simplicity and high resolution, experimentation can be easily performed at localized regions (~ few nm region to single atomic column) in a transmission electron microscope, while XANES requires synchrotron x-ray source. However, quantitative EELS simulations have been very difficult due to computational difficulty to generate spectra closely resembling with experimental counterpart. Fingerprinting in EELS is widely used to compare absorption edge spectra for an element in various compounds to derive any inferences qualitatively. WIEN2K based TELNES2 programme, which uses a fully relativistic equation for double differential cross section (in a TEM at 300 kV, the speed of electron is 0.88*c,*where *c* is the speed of light in vacuum), have been used to calculate EELS spectra of various oxygen deficient wurtzitic ZnO lattice. Also it was found that core-hole consideration (which necessitates large supercells to reduce interactions between coreholes and hence is computationally expensive) is not compulsory to qualitatively study the evolutions of the pre-edge absorption peaks. TELNES2 programme calculates EELS spectra up to nearly 50 eV from the core edge absorption threshold fairly well. In the present work we have studied basically the pre-edge feature at core absorption edges Zn L_3 and O K of both experimental and theoretical spectra.

Although it is possible to quantify oxygen occupancy in a given crystal lattice by HRTEM, applying the same method to nanocrystalline material form is extremely difficult (as it involves tilting the nanocrystals towards zone axis orientation and they are not stable for sufficiently large time under electron beam exposure). Therefore we have studied the defect structure in ZnO through observation of core absorption edge ELNES and emphasis is given to any changes in the pre edge feature.

3.5. Methods

3.5.1. Experimental methods

The synthesis of ZnO nanoparticles has been done by using a previously reported procedure [41]. The method is hydrolysis of zinc acetate in methanol using KOH. In a typical synthesis, zinc acetate (0.01 mol) was dissolved in methanol (125 mL) under vigorous stirring at about 333 K . Subsequently, a solution of KOH (0.03 mol, 65 mL) in methanol was added drop wise at 333 K. The reaction mixture was stirred for 6 h at 333 K. The white precipitate thus obtained was harvested by centrifugation and washed thoroughly with HPLC ethanol and air-dried at 313 K. Thus obtained ZnO nanoparticles were annealed in a 500 Standard cubic centimeter per minute (sccm) oxygen flow at different temperatures like 200°C and 400°C for 10 hours to obtain particles with different sizes.

The PL spectra of the nanocrystals were recorded with a Perkin–Elmer LS55 luminescence spectrometer. Electron energy loss near edge structures were acquired using a gun monochromator (both in image and diffraction mode) in a FEI-TITAN^{3TM} 80-300 kV transmission electron microscope operating at 300 kV. In order to improve the signal over noise, camera length and energy dispersion scale were reduced to 73 mm and 0.03 eV/pixel respectively, which reduces the energy resolution from 0.18 to 0.28 eV as measured from full width at half maxima (FWHM) of zero loss peak (ZLP). Gatan imaging filter (GIF) entrance aperture size of 1 mm was chosen which ensured high energy resolution during spectra acquisition. Near edge structure up to 50 eV from the absorption edge for both O K and Zn L_3 edge were acquired for samples with different oxygen vacancy concentrations and emphasis was given to changes in the features at the onset of absorption edge.

3.5.2. Calculation methods

The density of states (DOS) and ELNES (with TELNES2 program in Wien2k) with a full potential linear augmented plane wave (FPLAPW) basis were calculated to study the changes in density of states with oxygen vacancy concentrations and respective ELNES spectra both for O K and Zn L_3 edges. The generalized gradient approximation (GGA) was employed with Perdew-Burke-Ernzenhof (PBE) functional. Four cases were studied:

(i) ZnO with no vacancies,

(ii) 6.25% O vacancies simulated with a super cell of ZnO (16 Zn, 16 O, 2×2×2 unit cell) with 1 O atom removed

(iii) 12.5% O vacancies simulated with a super cell of ZnO (8 Zn, 8 O, 2×2×1 unit cell) with 1 O atom removed, and

(iv) 25% O vacancies simulated with a super cell of ZnO (4 Zn, 4 O, 2×1×1 unit cell) with 1 O atom removed,

Wurtzite structure with space group $P6_3mc$ was generated with lattice parameters of minimum energy a=3.2973 Å and c = 5.2824 Å and atomic positions given by Zn (2/3, 1/3, 0), O (2/3, 1/3, u) and u = 0.3775 were used. Atomic positions of all the structures were relaxed internally using force minimization (using the minimization program *min_lapw*). Following values were used for various simulation parameters: Muffin-tin radii R_{mt} = 2.00 a.u. and 1.77 a.u. for Zn and O atoms respectively, the valence and core states were separated by -6.0 *Ry* of energy, and $Rk_{(max)}$ $\{(R_{mt(min)} * k_{max})\}$= 7.00. Integration over irreducible Brillouine zone with uniform 15×15×9 mesh of k points was done. Instrumental broadening of 0.2 eV, collection angle ~2.5 mrad, and convergence angle of ~0 (parallel illumination) were used in the input of TELNES2 program for a meaningful comparison between the theoretical and experimental spectra.

3.6. Results and Discussions

Figure 3 shows HRTEM images from three different ZnO nanocrystals. The average size of as synthesized ZnO nanocrystals, annealed at 200 °C and 400° C are 12 (± 3), 22 (± 5), and 33 (± 5) nanometers respectively. An increase in annealing temperature has caused an increase in crystal sizes.

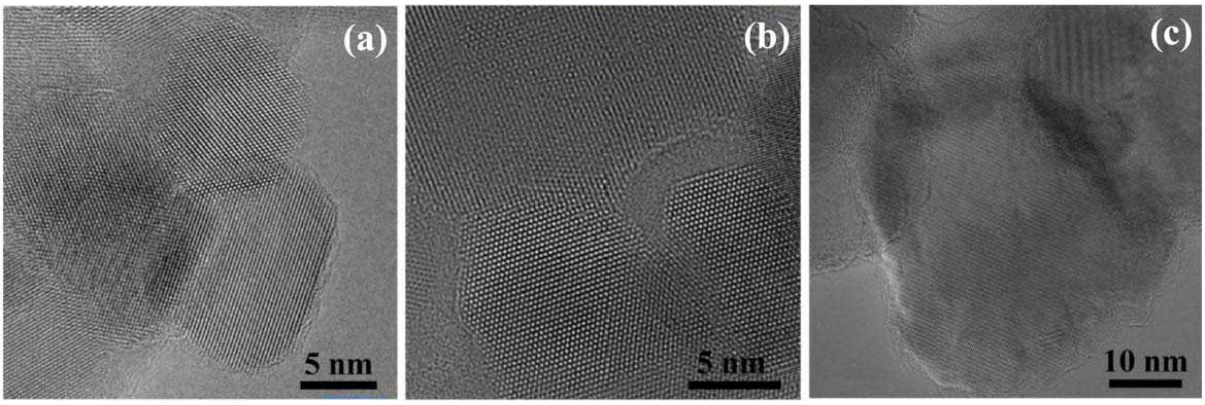

Figure 3: ZnO nanocrystals; (a) as synthesized at room temperature, (b) annealed at 200 °C and, (c) annealed at 400 °C under oxygen.

All the ZnO nanocrystals have wurtzite structure and the crystal structure remained unaltered upon annealing at various temperatures as evident from both electron and powder X-ray diffraction data (Figure 4).

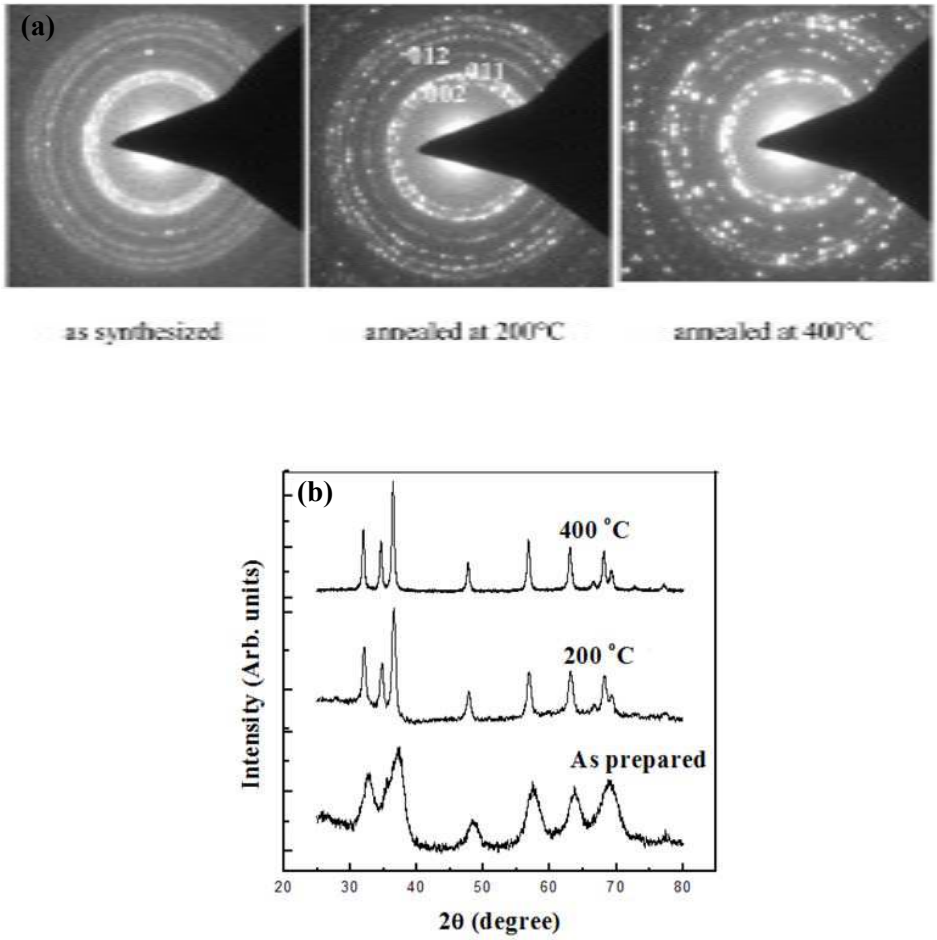

Figure 4:(a) Electron diffraction pattern from three different samples showing no change in hexagonal wurtzitic structure. (b) Powder X-ray diffraction pattern from three different samples showing no change in hexagonal wurtzitic structure. There is gradual broadening in the spectra coming from 400°C annealed sample to as prepared crystals due to decreasing crystal size in the order 400°C, 200°C, as prepared.

The photoluminescence of three different ZnO nanocrystals (see Figure 5) are given. One can clearly observe that green emission is quite intense and broad for as synthesized ZnO sample and it is getting quenched as we go to 200°C and 400°C annealed samples.

This is suggestive that green emission may be related to oxygen vacancies in ZnO and quenched significantly by annealing which might have replenished oxygen in the ZnO lattice.

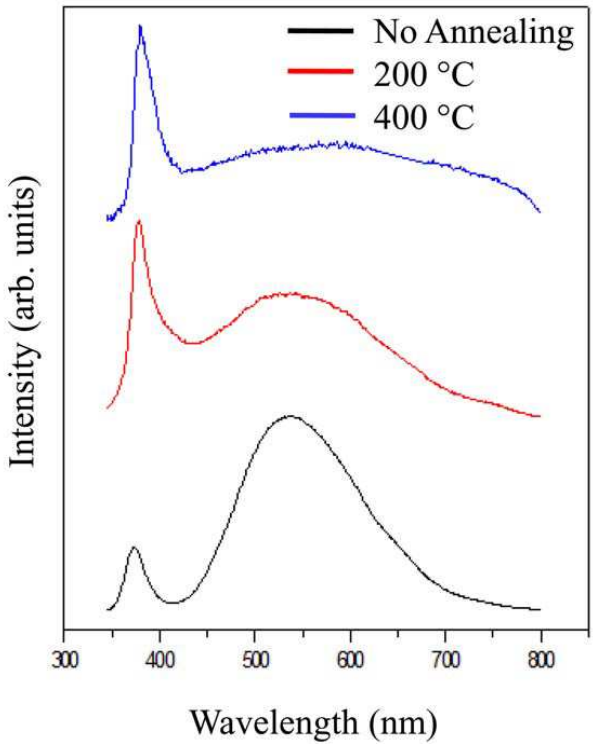

Figure 5: Photoluminescence from the samples

From experimental ELNES spectra and its first derivative of O K edge (figure 6), one observes that the fine features in the spectra are washed out in O K but there are no appreciable changes at pre-edge features as a function of O vacancies. O atoms come only in the second co-ordination shell of any O vacancy, may be this is the reason for the absence of pre-edge features in O K edge.

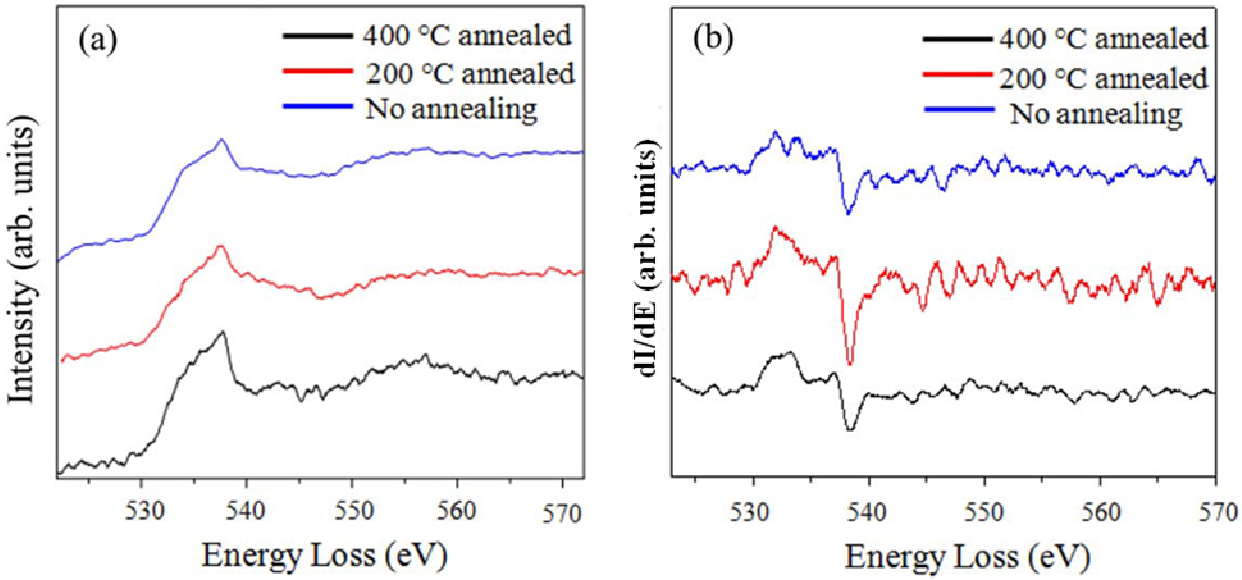

Figure 6:(a) Experimental O Kedge ELNES and (b) its first derivative. The pre-edge features are not clear in this case.

In contrast, there are clear pre-edge features for the three samples in the Zn L_3 spectra. The four main expected peaks of ZnO are labeled A, E, T and TT in Figure 7. The relative peak height of *b* to *a* is increasing with oxygen vacancy concentrations. There are also extra peaks like *c*, *d* etc. that come up at higher oxygen deficiencies. The ratio of *b* to *a* increases marginally (0.23 to 0.5) with increasing concentrations of oxygen deficiencies. The changes in the pre-edge structures have been made very prominent by plotting the derivative spectra.

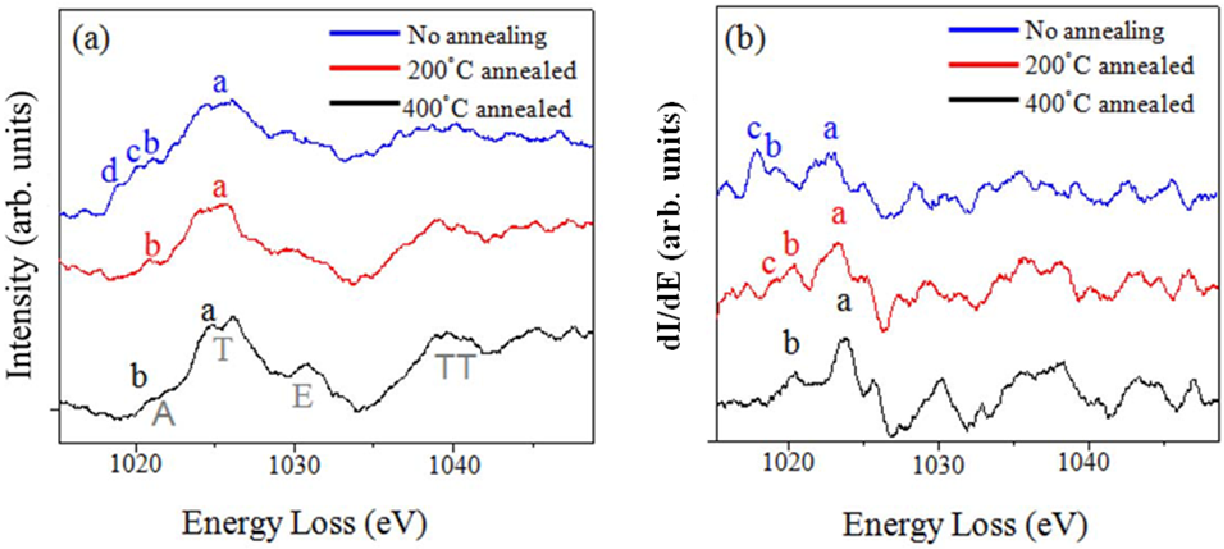

Figure 7:(a) Experimental Zn L_3 edge ELNES and (b) its first derivative. The pre-edge features are labeled.

Experimental spectra are compared with theoretical ELNES to understand better the changes in the pre-edge structure with increasing oxygen vacancy defects in terms of change in the unoccupied electronic density of states. Figure 8 (a) and (b) show theoretical ELNES spectra of O K and Zn L_3 edge respectively of ZnO with different oxygen vacancy concentrations (i.e. no vacancy, 6.25%, 12.5% and 25%).

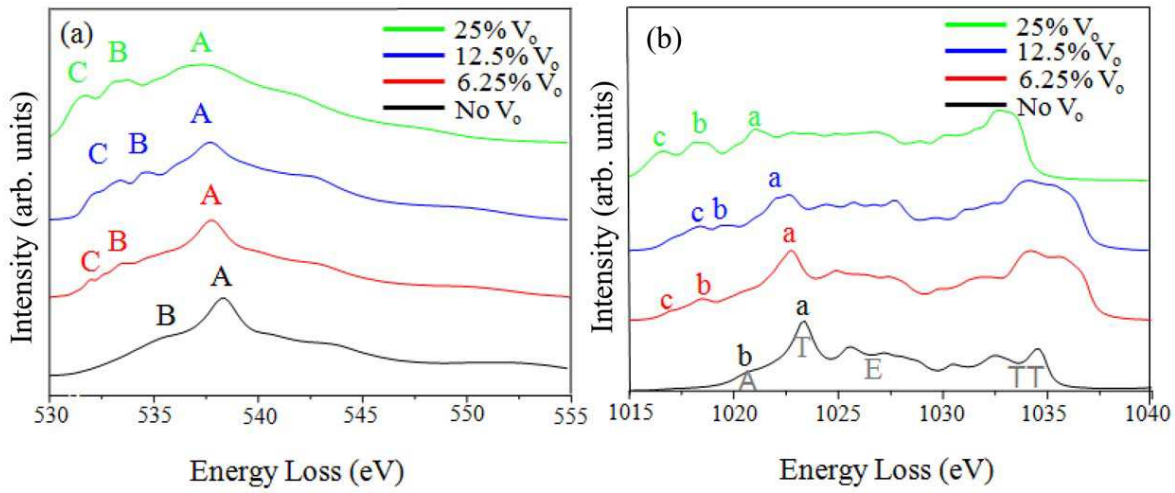

Figure 8: Theoretical DFT calculation of ELNES spectra of (a) O K edge and (b) Zn L_3 edge for various oxygen vacancy concentrations.

One interesting feature in these spectra is the appearance of pre edge feature with the oxygen vacancy (V_O) introduced in the ZnO lattice. Peaks A and B in both O K and Zn L_3 edges arise from p unoccupied levels of O hybridized with 4s levels of Zn. The peak B and additional peak C become more prominent with increasing V_O. Additionally, ratio between peak B/peak A increases with increasing V_O concentrations. One makes similar observation in the Zn L_3 pre-edge structure. EELS spectrum provides information about density of un-occupied states which is related to local atomic environments. Therefore, ELNES of both O K and Zn L_3 with unoccupied partial-DOS have been plotted in the same graph to relate the ELNES peaks with corresponding DOS in Figure 9. One can notice that as oxygen vacancy increases from 0% to 25%, all the partial density of states redistributes in the energy band gap. These defect related

donor levels contribute to the pre-edge peaks in the spectra and same effect is observed on both the absorption edges.

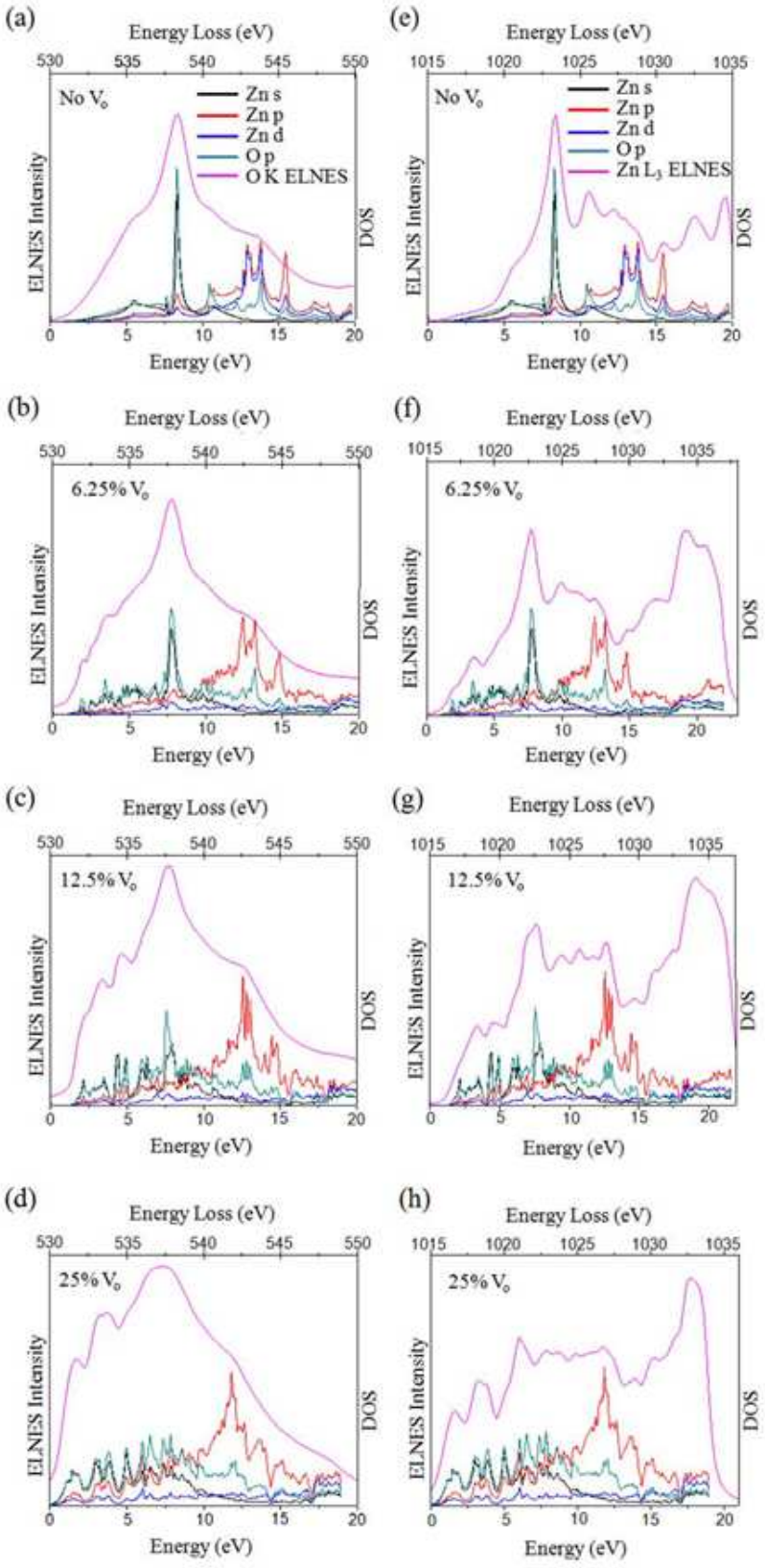

Figure 9: Superposed plot of ELNES and DOS for (a)-(d) O K and (e)-(h) for Zn L_3 edge.

Although such high concentrations of oxygen vacancies is unrealistic (i.e. 25%, 12.5 % etc.) in practical w-ZnO lattice, calculations have been helpful in understanding the resulting trend in change in electronic structure and its reflection in EEL spectra. Indeed, it was quite a successful attempt to a very good extent since we could see the similar trends in the Zn L_3 experimental and theoretical spectra as the oxygen vacancy concentration is increased (illustrated in Figure 10).

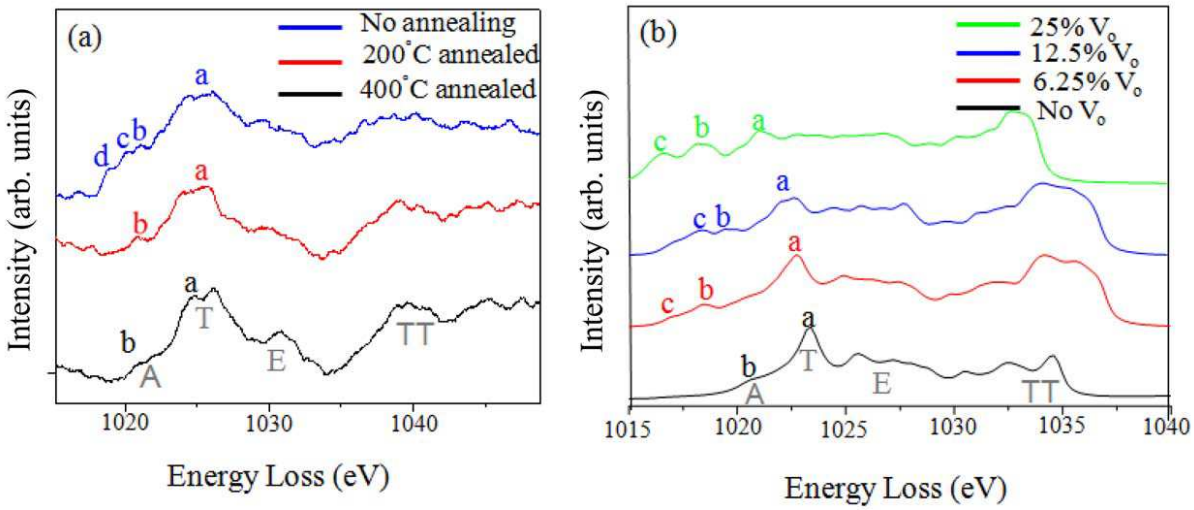

Figure 10:A comparison between (a) experimental and (b) computed spectra for Zn L_3 edge.

A small change in pre-edge structure in our experimental spectra indicates that a more realistic estimate of V_O concentrations value would be within few percent. As it is still not clear that the origin of green emission in ZnO is truly from oxygen vacancy or some other type of defects, it will be useful to calculate ELNES spectra for various types of native point defects possible in ZnO lattice as well as different vacancy complexes to reach a firm conclusion on the assignment of a mechanism responsible for green emission, and by looking not only at the pre-edge feature but at near edge structure as well.

3.7. Conclusions

In conclusion, the experimental ELNES pre-edge structures of three different ZnO nanocrystals with different oxygen defect concentrations have been compared. Broadening of the main peak in experimental absorption edge both in O K and Zn L_3 was observed with increasing oxygen vacancies. From theoretical ELNES spectra, the appearance of extra peaks with increasing density of Vo in ZnO nanocrystals were observed, similar to the feature observed at Zn L_3 pre edge structure experimentally. These features are due to donor levels in the band gap arising from oxygen defects.

References

1. C. Kligshirn, *Phys. Status Solidi B* **71**, 547 (1975).
2. *Numerical Data and Fundamental Relationships in Science and Technology*, Vol. 17 of Landolt-Bornstein new series ~Springer-Verlag, Berlin, 1982).
3. J. Bian, W. Liu, J. Sun, and H. Liang, J. Mater. Process. Tech. **184**, 451 (2007).
4. D. M. Bagnall, Y. F. Chen, Z. Zhu, T. Yao, S. Koyama, M. Y. Shen, and T. Goto, Appl. Phys. Lett. **70**, 2230 (1997).
5. S. Nakamura and S. F. Chichibu (ed) *Nitride Semiconductor Blue Lasers and Light Emitting Diodes* (Boca Raton, FL: CRC Press) (2000)
6. Ü. Özgür, Ya. I. Alivov, C. Liu, A. Teke, M. A. Reshchikov, S. Doğan, V. Avrutin, S.-J. Cho, and H. Morkoç *J. Appl. Phys.* **98**, 041301 (2005).
7. D. C. Look, *Mater. Sci. Eng., B* **80**, 381 (2001).
8. D. C. Look, D. C. Reynolds, J. W. Hemski, R. L. Jones, and J. R. Sizelove, *Appl. Phys. Lett.* **75**, 811 (1999).
9. A. Y. Polyakov, N. B. Smirnov, A. V. Govorkov, E. A. Kozhukhova, V. I. Vdovin, K. Ip, M. E. Overberg, Y. W. Heo, D. P. Norton, S. J. Pearton, J. M. Zavada, and V. A. Dravin *J. Appl. Phys.* **94**, 2895 (2003).
10. O. Kucheyev, J. S. Williams, C. Jagadish, J. Zou, C. Evans, A. J. Nelson, and A. V. Hamza, *Phys. Rev. B* **67**, 094115 (2003).
11. X. Gu, M. A. Reshchikov, A. Teke, D. Johnstone, H. Morkoc, B. Nemeth, and J. Nause, *Appl. Phys. Lett.* **84**, 2268 (2004);
12. A. Janotti and C. G. Van de Walle, *Rep. Prog. Phys.* **72,** 126501(2009).
13. Lannoo M and J. Bourgoin *Point Defects in Semiconductors II: Experimental Aspects* (Berlin: Springer).(1983)

14. S. E. Harrison *Phys. Rev.* **93,** 52, (1954).

15. A.R. Hutson *Phys. Rev.* **108,** 222, (1957).

16. Thomas D G 1957 *J. Phys. Chem. Solids (USA),* **3,** 229, (1957).

17. C. G. Van de Walle, Phys. Rev. Lett. **85**,1012.

18. C. G.Van de Walle *Physica* B, 899, 308 (2001).

19. A.Janotti and C. G. Van de Walle, Appl. Phys. Lett. **87**, 122102 (2005).

20. A. Janotti and C. G. Van de Walle *J. Cryst. Growth,*, **58**, 287 (2006)

21. L. S. Vlasenko and G. D. Watkins, Phys. Rev. B **72**, 035203 (2005)

22. T. Dietl, H. Ohno, F. Matsukura, J. Cibert, and D. Ferrand, Science **287**,1019 (2000).

23. T. Dietl, *Nat. Mater.* 9, 965 (2010).

24. J.M.D. Coey, M. Venkatesan, C.B. Fitzgerald, *Nat. Mater.* **4**, 173 (2005).

25. F. Oba, A. Togo, I. Tanaka, J. Paier and G. Kresse *Phys. Rev.* B **77** 245202 (2008).

26. R. Vidya, P. Ravindran, H. Fjellvag, B. G. Svensson, E. Monakhov, M. Ganchenkova, and R. M. Nieminen *Phys. Rev. B* **83**, 045206 (2011).

27. P. Redlich, D. L. Carroll, and P. M. Ajayan *Curr. Opin. Solid State. Mater. Sci.* **4**,325 (1999).

28. J. C. H. Spence *Rep. Prog. Phys.* **69**,725 (2006).

29. W. Grogger, F. Hofer, G. Kothleitner, and B. Schaffer *Top. Catal.* **50**,200 (2008).

30. C. B. Carter, and D. B. Williams, *Transition Electron Microscopy: A Text Book for Materials,* 2nd edition, Springer (2009).

31. C. L. Dong, C. Persson, L. Vayssieres, A. Augustsson, T. Schmitt, M. Mattesini, R. Ahuja, C. L. Chang, and J.H. Guo, *Phys. Rev. B* **70**, 195325 (2004).

32. C. Ton-That, M. R. Phillips, M. Foley, S. J. Moody, and A. P. J. Stampfl, *Appl. Phy. Lett.* **92**, 261916 (2008).

33. R. M. Dreizler, and E. K. U. Gross *Springer-Verlag, New York* (1991).

34. P.C. Hohenberg, W.Kohn, and L. J. Sham *J. Adv. Quant. Chem.* **21**, 7 (1990).

35. W. Kohn, and L. J. Sham, *Phys. Rev.* **140**, A1133 (1965).

36. D. M. Ceperley, and B. J. Alder, *Phys. Rev. Lett.* **45**, 566 (1980).

37. J. P. Perdew, and Y. Wang, *Phys. Rev. B* **45**, 13244 (1992).

38. K. Burke, The ABC of DFT (2001).

39. J. P.Perdew, M.Ernzerhof, A. Zupan, and K. Burke *J. Chem. Phys.* **108**, 1522, (1998).

40. K. Jorissen, PhD thesis, University of Antwerp (2007).

41. L. S. Panchakarla, Y. Sundarayya, S. Manjunatha, A. Sundaresan, and C. N. R. Rao, *ChemPhysChem* **11**, 1673 (2010).

42. H. S. Hsu, J. C. A. Huang, Y. H. Huang, Y. F. Liao, M. Z. Lin, C. H. Lee, J. F. Lee, S. F.Chen, L. Y. Lai, and C. P. Liu, *Appl. Phy. Lett.* **88**, 242507 (2006).

43. D. A. Muller, N. Nakagawa, A. Ohtomo, J. L. Grazul & H. Y. Hwang, *Nature* **430**, 657 (2004).

44. C. L. Jia, M. Lentzen, and K. Urban, *Science* **299**, 870 (2003).